Computational Model for Wave Attenuation by Flexible Vegetation

Steven A. Mattis[1]; Christopher E. Kees[2]; Maya V. Wei[3]; Aggelos Dimakopoulos[4]; and Clint N. Dawson[5]

Abstract: Coastal vegetation has a well-known effect of attenuating waves; however, quantifiable measures of attenuation for general wave and vegetation scenarios are not well known, so field and laboratory studies must be performed for individual setups. The standard practice of performing these studies for such scenarios is extremely expensive, and it is difficult to change parameters and setups. We presented and validated a computational model for a wave flume that can be used for studies of wave attenuation over flexible vegetation based on the previously developed immersed-structure method for fluid–vegetation interaction, thereby augmenting field and laboratory studies with a more-flexible and less-expensive alternative. The main advantage of this computational framework is that almost all terms are derived from first principles without requiring a large number of empirically determined parameters. A series of computational experiments were performed, and an analysis of the wave attenuation with respect to wave heights, spectra, and energy was conducted. Results were compared to results from experiments that the computational wave flume was designed to replicate. **DOI: 10.1061/(ASCE)WW.1943-5460.0000487.** *© 2018 American Society of Civil Engineers.*

Introduction

Flow in coastal regions is complicated by the presence of smaller-scale features, including barrier islands, dikes, levees, and vegetated marshlands. Coastal vegetation, perhaps the smallest scale of these features, is one of the most important, affecting surface flow by causing resistance to the flow, altering turbulence characteristics, increasing mixing, and attenuating waves. The ability of coastal vegetation to attenuate waves is of particular interest to protecting coastal resources from waves associated with high-energy storm events. Wave attenuation can be quantified in a variety of ways, as vegetative obstacles affect wave heights, wave spectra, and wave energy differently. Wave attenuation due to vegetation has been studied with field experiments, laboratory experiments, and computational models.

Performing field experiments during such storm events to measure the effect of vegetation has proven to be difficult, so there have been relatively few studies. In the studies that have been done, such as by Krauss et al. (2009), Smith et al. (2011), and Jadhav et al. (2013), the amount of fine-scale spatial data is limited, because the research was mostly interested in bulk characteristics. There have been a significant number of field studies on the effects of coastal vegetation on lower-energy wave events. Early work by Wayne (1976) and Knutson et al. (1982) studied dissipation within vegetated regions, with the latter noticing a significant amount dissipation—a 94% wave-height reduction over 30 m. Möller and Spencer (2002) noticed much greater wave dissipation over salt marshes than unvegetated mudflats, and Cooper (2005) found double the wave attenuation in salt marshes than mudflats. Quartel et al. (2007) found that wave attenuation in a coastal mangrove system was much greater than by solely bottom friction. These studies showed the significant impact of vegetation on wave attenuation; however, as pointed out by Mendez and Losada (2004), there is a great deal of variability in the results because of the complex dynamics in the water-vegetation system.

Because of the difficulty and expense of field experiments, many laboratory experiments have studied wave–vegetation interaction. It is much easier to control the conditions in a laboratory setting to study the effects of different parameters. Such experiments have often used artificial vegetation to model the effects of real vegetation (Lowe et al. 2007; Dubi and Tørum 1996; Lima et al. 2007; Mei et al. 2011; Sánchez-González et al. 2011; Stratigaki et al. 2011; Anderson and Smith 2014; Manca et al. 2012; Koftis et al. 2013; Wu et al. 2011), as well as live plants (Fonseca and Cahalan 1992; Augustin et al. 2009; Wu et al. 2011). As with field experiments, these laboratory experiments demonstrated the great capacity of vegetation to attenuate waves; however, the amount of attenuation varied greatly. The contribution of wave setup to the amount of attenuation was addressed by Anderson and Smith (2014), who analyzed a physical model of *Spartina alterniflora*.

Laboratory wave-attenuation studies are extremely expensive to perform and require large testing facilities. There are several theoretical models of wave-energy dissipation caused by vegetation based on theoretical and empirical relationships (Chen and Zhao 2012; Zhu and Chen 2017). Recently, computational models have been developed to model the interaction of surface water flow with flexible vegetation. A common approach in these studies, proposed by Kutija and Thi Minh Hong (1996), is to model vegetation as simple cantilever beams. Approaches to the actual stem and vegetation mechanics are discussed here. In general, these models involve

---

[1] Postdoctoral Researcher, Zentrum Mathematik, Technical Univ. of Munich, Garching 85748, Germany (corresponding author). Email: mattis@ma.tum.de

[2] Research Hydraulic Engineer, Coastal and Hydraulics Laboratory, US Army Engineer Research and Development Center, 3909 Halls Ferry Rd., Vicksburg, MS 39180.

[3] Student, Institute for Computational Engineering and Sciences, Univ. of Texas at Austin, 201 East 24th St., Stop C0200, Austin, TX 78712.

[4] Senior Engineer, HR Wallingford, Howbery Business Park, Crowmarsh Gifford, Wallingford, OX10 8BA, UK.

[5] Professor, Institute for Computational Engineering and Sciences, Univ. of Texas at Austin, 201 East 24th St., Stop C0200, Austin, TX 78712.

Note. This manuscript was submitted on October 18, 2017; approved on June 21, 2018; published online on October 18, 2018. Discussion period open until March 18, 2019; separate discussions must be submitted for individual papers. This paper is part of the ***Journal of Waterway, Port, Coastal, and Ocean Engineering***, © ASCE, ISSN 0733-950X.

J. Waterway, Port, Coastal, Ocean Eng., 2019, 145(1): 04018033

coupling a model for vegetation deflection with either a Reynolds-averaged Navier-Stokes (RANS) or large-eddy simulation (LES) technique to model the flow. RANS approaches require solving a transport system modeling the creation and dissipation of turbulent kinetic energy, which can be used to calculate additional fluid stress due to turbulence. In LES, some of the turbulent effects are considered by the numerical solution, whereas the subgrid turbulent effects are modeled.

Two-dimensional (2D) LES simulations of this type of model were performed by Ikeda et al. (2001). Erduran and Kutija (2003) used a three-dimensional (3D) RANS technique with a combination of mixing length and eddy viscosity turbulence closure schemes. They also proposed a quasi-3D coupling with shallow-water equations. Li and Xie (2011), building on work involving stiff vegetation by Li and Zeng (2009), added to the flexible-vegetation model by assuming a thin plate of *foliage* and used a 3D LES scheme with Smagorinsky's turbulence closure. Dijkstra and Uittenbogaard (2010) incorporated similar techniques for flexible vegetation with foliage using a RANS model. Recently, Chen et al. (2016b) performed numerical studies of wave propagation over a vegetated platform. An alternative to direct numerical modeling of the plant dynamics is to incorporate the interaction between waves and flexible vegetation into a 2D RANS-type model using semiempirical models for flexible plant dynamics and energy dissipation due to vegetation, as proposed by Hiraoka and Ohashi (2008) and Maza et al. (2013). These models have been shown to accurately reproduce certain 2D experimental data; however, they require several empirical parameters, including bulk drag coefficients and up to eight coefficients for k-ϵ and k-ω closure schemes, which must be tuned for specific flow and wave situations.

The common approach for computationally modeling individual pieces of flexible vegetation is by treating a piece of vegetation as a flexible cantilever beam. Kutija and Thi Minh Hong (1996) first proposed this method using the standard Timoshenko's beam theory (Timoshenko 1956), and similar approaches have been used by Saowapon and Kouwen (1989), Darby (1999), Erduran and Kutija (2003), Ikeda et al. (2001), Velasco et al. (2008), Kubrak et al. (2012), Li and Xie (2011), and Luhar and Nepf (2016). Zhu and Chen (2015) presented a method for flexible vegetation and wave coupling involving a force balance and a variety of wave models. All of the aforementioned methods only consider planar bending; however, in a flow with large velocity or a great deal of directional change or turbulence (e.g., a wave series), we would not expect planar bending. Many of these models are only valid for relatively small deflections; however, Luhar and Nepf (2011, 2016), Zhu and Chen (2015), Zeller et al. (2014), Chen et al. (2016a), and Tahvildari (2017) developed models to handle large deflections. We used an approach, first shown by Mattis et al. (2015), that was designed for modeling flexible vegetation as cantilever beams in a way that allows for large 3D deflections and is as robust and accurate as possible but is not overly computationally expensive. A similar formulation was created by Luhar and Nepf (2011) for blades and was later used to study wave-induced dynamics (Luhar and Nepf 2016) using a different fluid–vegetation interaction model. The advantage of these models is that they require very few modeling assumptions and empirical parameters to model the deflection of vegetation, unlike the methods incorporating vegetation into RANS closure schemes. The numerical methods for individual beam deflection are robust and extremely cheap to implement and allow for complex plant layouts and geometries without being a computational burden. The coupling between fluid flow and vegetation deflection is done in a novel way, incorporating ideas from the immersed boundary method and implicitly conserving momentum. The coupling requires very few restrictions on the discretization of the system.

In this paper, we present a computational model for wave–vegetation interaction that requires few extra assumptions. A previous method developed by Mattis et al. (2015) for modeling the interaction of incompressible fluids and flexible vegetation with an immersed-structure method was applied to a wave-flume setup. We developed a computational wave flume, reproducing the experimental setups by Anderson and Smith (2014). The geometry and parameters of these wave setups are described in detail here followed by an explanation of the computational modeling framework and methodology. An analysis of wave-height attenuation, wave-spectrum attenuation, and wave-energy attenuation was performed on the results from the computational experiments, and the results were compared to the experimental results from Anderson and Smith (2014). Such computational frameworks have the potential to be applied to many wave/vegetation setups quickly and cheaply.

Experimental Methodology

In this work, we developed a computational wave flume modeled on a real-world wave flume at the US Army Engineer Research and Development Center in Vicksburg, Mississippi. The flume was used by Anderson and Smith (2014) to study wave attenuation by flexible, idealized salt-marsh vegetation. We replicated their experimental setups as accurately as possible and compared the results to those from the experiments. A full list of parameters of interest for the wave setups are shown in Table 1.

A cross section of the flume is shown in Fig. 1. The flume is 63.4-m long, 1.5-m wide, and 1.5-m deep, with a wave generator on one end and a sloped area of foam padding on the other end to absorb the waves and minimize reflection. At the wave generator, the flume is 0.45 m deeper for a section 2.4 m long. This region is followed by a gradual 1:44 slope for 17.2 m, followed by a 1:20 slope for 6.1 m. Next, there is a flat platform for 12.2 m. The middle 9.8 m of this region contains the idealized vegetation. The flat platform is followed by a 1:20 slope with absorbers made from filtration media.

Anderson and Smith (2014) created idealized vegetation to simulate the basic morphology of *Spartina alterniflora*, a common grass in salt marshes. The simulated vegetation was made from 0.0064-m-diameter (b_v) cross-linked polyolefin (XLPO) tubing cut into pieces 0.415 m in length (l_v). The XLPO had a density of 1,350 kg/m^3 and an approximate Young's modulus (E_v) of

Table 1. Symbols and units for values of interest

Parameter	Symbol	Unit
Mean water depth	h	m
Zero-moment wave height	H	m
Root-mean-square wave height	H_{rms}	m
Incident wave height	H_0	m
Peak period	T_p	s
Peak wavelength	L_p	m
Vegetation height	l_v	m
Vegetation diameter	b_v	m
Frequency	f	Hz
Spectral density	S	m^2 s
Wave decay coefficient	k_i	m^{-1}
Drag coefficient	C_D	—
Stem density	N	stems/m^2
Reynolds number	R	—
Keulegan-Carpenter number	KC	—

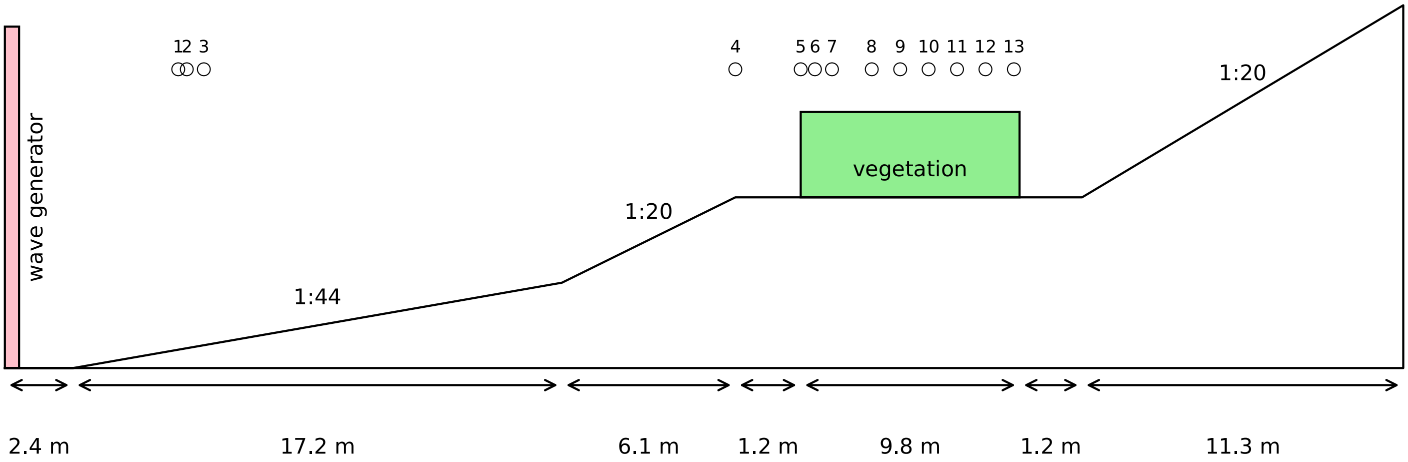

Fig. 1. Cross section of the flume setup.

172.4 MPa. Although the stem density and arrangement vary greatly in a real-life bed of vegetation, they chose three setups of regularly arranged stems with different stem densities (N). The first was a control arrangement with no vegetation ($N = 0$ stems/m^2). The others had stem densities of $N = 200$ and 400 stems/m^2, which corresponded to grid spacings of 0.071 and 0.050 m, respectively. The stems in these cases were arranged in the pattern shown in Fig. 2.

The waves were generated using a computer-controlled electrohydraulic piston wave generator. A Texel, Marsen, and Arsloe (TMA) shallow-water wave spectrum with spectral peakedness of $\gamma = 3.3$ was used to generate 15 single-peaked irregular wave conditions. Anderson and Smith (2014) systematically varied incident wave height and peak period to study their effects on wave dissipation. Note that the total and incident wave heights were assumed to be practically equal. Wave reflection in the flume was anticipated to be negligible due to the relatively mild beach slopes and the low effective solid fraction of the vegetation. Reflection coefficients were measured between 8.2 and 8.7%. Peak period (T_p) varied from 1.25 to 2.25 s, and incident wave height (H_0) varied from 0.050 to 0.192 m. Also, a variety of mean water depths (h) were used, allowing for emergent vegetation ($l_v > h$) and submerged vegetation ($l_v < h$). Waves were generated for 480 s to ensure proper statistics. A summary of the parameters for the setups is shown in Table 2. The time series of water heights were measured at 13 locations using single-wire capacitance-type wave gauge (WG) sampling at 25 Hz. The locations for WGs 1–13 with respect to the wave generator were 6.1, 6.4, 7.0, 26.0, 26.9, 27.4, 27.9, 28.5, 29.5, 31.0, 32.7, 34.4, and 36.2 m in the center of the flume. Note that WG 4 was at the beginning of the vegetation platform, WG 5 was at the beginning of the vegetation, and WGs 6–13 were within the vegetated region. Anderson and Smith (2014) performed a full analysis of wave attenuation with the wave-height data, and we were given access to the data. We reproduced these experimental setups computationally with the methodology presented in the following section.

Modeling Framework

In this section, we present the modeling framework for the computational wave flume. This framework required several parts. First, we generated plane random waves using linear reconstructions of components from known wave spectra associated with the parameters in Table 2. We assumed the well-known TMA shallow-water wave spectrum, a variation of the JONSWAP spectrum. Wave heights and velocities were reconstructed following the method presented by Gōda (2010). Another part was modeling the fluid flow in the wave flume based on the wave series. A third part was modeling the flexible vegetation, which is the main cause of the wave attenuation. Finally, the interaction between the fluid flow and the flexible vegetation must be considered. The fluid–vegetation interaction was modeled with an immersed structure approach originally developed by Mattis et al. (2015).

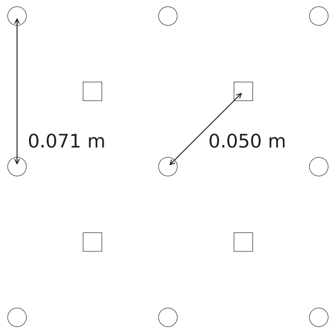

Fig. 2. Arrangement of idealized vegetation in the x,y-plane in the numerical model and experiments. The circles indicate the case of $N = 200$ stems/m^2, and the squares indicate the additional stems for $N = 400$ stems/m^2.

Modeling Wave Series with a Two-Phase Flow Model

LES-type models have been previously been found useful for predicting wave dissipation (Hieu et al. 2004; Christensen 2006; Dimakopoulos and Dimas 2011). The most common type of LES is based on the incompressible Navier-Stokes equations

$$\nabla \cdot \mathbf{v} = 0$$
$$\frac{\partial \mathbf{v}}{\partial t} + \nabla \cdot \left(\mathbf{v} \otimes \mathbf{v} - (\nu + \nu_T) S_{ij} \right) + \frac{\nabla p}{\rho} - \mathbf{f} = 0 \tag{1}$$

where $\mathbf{v}$ = velocity; p = pressure; $\mathbf{f}$ = body forces; ρ = density; ν = kinematic viscosity; and ν_T = turbulent viscosity. In the situations that are of interest, turbulence is a major concern. To capture the large-scale effects of turbulence without the need to resolve smaller turbulence length scales, we used Smagorinsky's model, a form of LES. Smagorinsky's model assumes the eddy viscosity (ν_T) satisfies

Table 2. Wave parameters for the 15 different setups

Run number	Depth [h (m)]	Wave height [H_0 (m)]	Peak period [T_p (s)]	Peak wavelength [L_p (m)]	l_v/h	H_0/h	h/L_p
1	0.533	0.111	1.5	2.89	0.78	0.21	0.18
2	0.533	0.110	1.75	3.53	0.78	0.21	0.15
3	0.533	0.112	2.0	4.16	0.78	0.21	0.13
4	0.457	0.081	1.5	2.74	0.91	0.18	0.17
5	0.457	0.109	1.5	2.74	0.91	0.24	0.17
6	0.457	0.139	1.5	2.74	0.91	0.30	0.17
7	0.457	0.050	2.0	3.91	0.91	0.11	0.12
8	0.457	0.107	2.0	3.91	0.91	0.23	0.12
9	0.457	0.153	2.0	3.91	0.91	0.33	0.12
10	0.457	0.192	2.0	3.91	0.91	0.42	0.12
11	0.305	0.113	1.25	1.88	1.36	0.37	0.16
12	0.305	0.110	1.5	2.36	1.36	0.36	0.13
13	0.305	0.112	1.75	2.82	1.36	0.37	0.11
14	0.305	0.111	2.0	3.28	1.36	0.36	0.09
15	0.305	0.112	2.25	3.73	1.36	0.37	0.08

$$\nu_T(\mathbf{x}) = \left(C_s \Delta_g\right)^2 \sqrt{2 S_{ij} S_{ij}} \tag{2}$$

where the filter size [Δ_g (m)] is set to the computational grid size; C_s = Smagorinsky's constant; and

$$S_{ij} = \frac{1}{2}\left(\frac{\partial v_i}{\partial x_j} + \frac{\partial v_j}{\partial x_i}\right) \tag{3}$$

is an entry of the filtered strain-rate tensor. The standard Smagorinsky's model takes C_s as a constant generally between 0.1 and 0.3; however, this assumes homogeneous isotropic turbulence and filter scale in the inertial subrange. We dealt with this type of turbulence as well as laminar flow, transitional flow, and sheared flows that do not have that structure. Voke (1996) and Meneveau and Lund (1997) presented practical methods for calculating C_s. By assuming a Pao turbulent energy spectrum, $C_s = 0$ for fully laminar flows, and for transitional and turbulent flows

$$C_s^2(\mathsf{R}_\Delta) = 0.027 \times 10^{-3.23 \mathsf{R}_\Delta^{-0.92}} \tag{4}$$

where $\mathsf{R}_\Delta = \left(\Delta_g^2 \sqrt{2 S_{ij} S_{ij}}\right)/\nu$ = mesh-Reynolds number at a given point in the flow. We used a locally conservative, stabilized finite-element method (Kees et al. 2009) to find weak solutions to the incompressible Navier-Stokes Eq. (1) using highly resolved unstructured tetrahedral meshes.

To model the wave flume hydrodynamics, we used a model for two-phase flow to model the full air–water system. We used a conservative level-set method (Kees et al. 2011). This method is designed for free-surface flow computations with complex phenomena, such as waves. It uses standard level-set methods with additional discrete conservation properties. Using the incompressible flow model [Eq. (1)] gives a water phase with density (ρ_w) and viscosity (ν_w) and an air phase with density (ρ_a) and ν_a, where ρ_a = 1.205 kg/m^3, ρ_w = 998.2 kg/m^3, $\nu_a = 1.5 \times 10^{-5}$ m^2/s, and $\nu_w = 1.004 \times 10^{-6}$ m^2/s. The boundary between the air and water phase (Γ) is represented by the zero level set of a function (ϕ)

$$\Gamma = \{\mathbf{x} | \phi(\mathbf{x}) = 0\} \tag{5}$$

As with standard level-set methods, the interface evolution is described by the level-set equation

$$\frac{\partial \phi}{\partial t} + \mathbf{v} \cdot \nabla \phi = 0 \tag{6}$$

where $\mathbf{v}$ = fluid velocity. The water lies in the region

$$\Omega_w = \{\mathbf{x} | \phi(\mathbf{x}) < 0\} \tag{7}$$

and the air lies in the region

$$\Omega_a = \{\mathbf{x} | \phi(\mathbf{x}) \geq 0\} \tag{8}$$

Using the method formulated by Kees et al. (2011), Eq. (6) is coupled with a volume fraction equation, a redistancing equation, and a level-set mass conservation equation, creating a conservative method. The redistancing step solves an eikonal equation, which makes ϕ a signed distance function. The density and viscosity near the interface are made continuous by using a regularized Heaviside function

$$H_\epsilon(\phi) = \begin{cases} 0 & \phi \leq -\epsilon \\ \frac{1}{2}\left(1 + \frac{\phi}{\epsilon} + \frac{1}{\pi}\sin\frac{\phi \pi}{\epsilon}\right) & |\phi| < \epsilon \\ 1 & \phi \geq \epsilon \end{cases} \tag{9}$$

where ϵ = small parameter. We take ϵ to be 1.5 times the local element diameter. Thus, ρ and ν are defined by

$$\rho = \rho_w H_\epsilon(\phi) + \rho_a(1 - H_\epsilon(\phi)) \tag{10}$$

and

$$\nu = \nu_w H_\epsilon(\phi) + \nu_a(1 - H_\epsilon(\phi)) \tag{11}$$

This method has been validated for several complicated fluid–structure interactions and wave scenarios (de Lataillade et al. 2017).

The two-phase flow model was applied to the wave flume by driving flow with boundary conditions. As mentioned earlier, we reconstructed time series of free surface elevations [ξ (x, t)] and velocities [$\mathbf{v_w}(x, y, z, t)$] based on wave spectra from input parameters. We used these series to define Dirichlet's boundary conditions for the flow and level-set models

$$\mathbf{v}(0, y, z, t) = \mathbf{v_w}(0, y, z, t) \tag{12}$$

$$\phi(0, y, z, t) = z - \xi(0, t) \tag{13}$$

We imposed no-flow boundary conditions on all other boundaries. We assumed a stationary initial condition with a level water surface, zero velocity, and hydrostatic pressure. All simulations were run in parallel on Texas Advanced Computing Center (TACC, Austin, Texas) machines using the Proteus Computational Methods and Simulation Toolkit (http://proteustoolkit.org). Simulations were run on 192 cores for times ranging from 40 to 48 h.

Modeling Flexible Vegetation as Beams

We modeled flexible vegetation as inextensible cantilever beams—beams that are anchored on exactly one end. The 3D cantilever beam is defined in terms of an arc-length parameter, $s \in [0, L]$, where L is the length of the beam, and it has a cylindrical cross section. We defined an orthonormal basis $\{\mathbf{e}_1(s), \mathbf{e}_2(s), \mathbf{e}_3(s)\}$, which describes the orientation of the beam's centerline at s and a vector $[\mathbf{r}(s)]$ that gives the position of the centerline at s in physical space using a Lagrangian framework. The position of the centerline of the beam can be described in terms of three Euler's angles (θ, ϕ, and ψ). E is Young's modulus, and I is the area moment of inertia about $\mathbf{e}_2$. G is the shear modulus, and J is the polar second moment of inertia about $\mathbf{e}_1$. Assume that the distributed load ($\mathbf{q} = [q_1, q_2, q_3]^T$) is a known function of spatial coordinates (x, y, and z) and that there are no end loads. Assuming Euler-Bernoulli beam theory, the potential energy of the beam is

$$E(\theta, \phi, \psi) = \int_0^L \left[\begin{array}{c} \frac{1}{2}\left(GJ\left(\psi'^2(1 + \cos^2\theta) + 2\psi'\phi'\cos\theta\right) + EI\left(\theta'^2 + \psi'^2\sin^2\theta\right)\right) \\ + Q_1 \sin\theta \cos\psi + Q_2 \sin\theta \sin\psi + Q_3 \cos\theta \end{array} \right] ds \tag{14}$$

where $q_1 = Q_1'$; $q_2 = Q_2'$; $q_3 = Q_3'$; and $Q_1(L) = Q_2(L) = Q_3(L) = 0$. Given a distributed load ($\mathbf{q}$), the static state of the beam is that which minimizes Eq. (14). We discretized the Euler's angles (θ, ϕ, and ψ) with quadratic finite elements and minimized Eq. (14) using Newton's method. Hence, given the load on the vegetation due to the fluid, we could calculate the position of the stem. The algorithm was described in detail by Mattis et al. (2015), including in-depth validation for large deflections.

Fluid–Vegetation Interaction

We have presented models for two-phase fluid flow to model traveling water waves and for the deformation of vegetation under distributed loads. To model the fluid–vegetation system, these models must be coupled. We formulated a fluid–structure interaction problem using the immersed-structure method. Assume that Ω is the domain for the two-phase flow model. Rather than just a single beam, we can have many beams (n_{beam}), with each modeling a piece of vegetation. B_k is the Lagrangian domain for the centerline of each beam, b_{v_k} is the diameter, and $\boldsymbol{\chi}_k$ is the mapping into Ω of the coordinates of beam k.

We used integral transforms to map between the Eulerian fluid framework and Lagrangian vegetation frameworks using an approach described by Peskin (2002). The integral transforms require an approximation to Dirac's delta

$$\delta_h(\mathbf{x}) = \frac{1}{h_{\text{mesh}}^3}\phi\left(\frac{x_1}{h_{\text{mesh}}}\right)\phi\left(\frac{x_2}{h_{\text{mesh}}}\right)\phi\left(\frac{x_3}{h_{\text{mesh}}}\right) \tag{15}$$

where h_{mesh} = beam element size; x_1, x_2, and x_3 = vector components of $\mathbf{x}$; and

$$\phi(r) = \begin{cases} 0, & r \le -2 \\ \frac{1}{8}\left(5 + 2r - \sqrt{-7 - 12r - 4r^2}\right), & -2 \le r \le -1 \\ \frac{1}{8}\left(3 + 2r + \sqrt{1 - 4r - 4r^2}\right), & -1 \le r \le 0 \\ \frac{1}{8}\left(3 - 2r + \sqrt{1 + 4r - 4r^2}\right), & 0 \le r \le 1 \\ \frac{1}{8}\left(5 - 2r - \sqrt{-7 + 12r - 4r^2}\right), & 1 \le r \le 2 \\ 0, & 2 \le r \end{cases} \tag{16}$$

The effect of drag due to the vegetative obstacles enters the fluid model as a momentum sink, and the effect of fluid flow enters the structure models as distributed loads in a way that conserves momentum. The bulk sink due to all of the beams is

$$\tilde{F}_i(\mathbf{x}) = \sum_{k=1}^{n_{\text{beam}}} F_i^k(\mathbf{x}) \tag{17}$$

where

$$F_i^k(\mathbf{x}) = -C_D^{\text{eff}}(\mathbf{x})\frac{1}{2}\rho(\mathbf{x})v_i^{\text{rel}}(\mathbf{x})\sqrt{v_j^{\text{rel}}(\mathbf{x})v_j^{\text{rel}}(\mathbf{x})}\int_{B_k} b_{v_k}\delta_h(\mathbf{x} - \boldsymbol{\chi}_k(s))ds \tag{18}$$

where v_i^{rel} = relative velocity between the fluid and vegetation; and C_D^{eff} = effective drag coefficient for the Reynolds numbers of interest for surface water flow (Hoerner 1965) for a single vegetative obstacle. For a single upright circular cylinder (the shape of the undeflected model vegetation), $C_D^{\text{eff}} \approx 1.2$ for R between 1.0×10^2 and 3.0×10^5. For bent stems, the drag coefficient must be adjusted. At each location along the bent obstacle, it is treated as an inclined circular cylinder. Hoerner (1965) experimentally showed that for most practical applications, the *cross-flow principle* holds in the case of an inclined cylinder. The principle states that the force acting in the direction normal to the axis of the cylinder can be expressed within terms of the normal component of the flow velocity only, and the axial direction is disregarded. If θ is the bent angle of the cylinder with respect to the vertical, then taking only the horizontal lift force gives an effective horizontal drag coefficient of $C_D^{\text{eff}} = 1.2\cos^3\theta$. The cross-flow principle has been confirmed for cases of inclined cylinders and bent wires, cables, and ropes. Drag coefficients for other common cross-sectional shapes are also generally well known for Reynolds numbers of interest and could be used for different cross-sectional shapes of obstacles without any tuning parameters. It is important to note that C_D^{eff} varies along the length of each individual beam based on its deflected shape. This type of deflection-dependent local drag assumption has a much different effect than simply assuming a bulk drag coefficient. The corresponding distributed load on beam k is

$$q_i^k(s) = C_D^{\text{eff}}(s)\frac{1}{2}b_{v_k}\int_{\Omega}\rho(\mathbf{x})v_i^{\text{rel}}(\mathbf{x})\sqrt{v_j^{\text{rel}}(\mathbf{x})v_j^{\text{rel}}(\mathbf{x})}\delta_h(\mathbf{x} - \boldsymbol{\chi}_k(s))d\mathbf{x} \tag{19}$$

For each time step of the two-phase flow model, we coupled the fluid–vegetation system. The fluid–structure coupling at time t_n was done by:

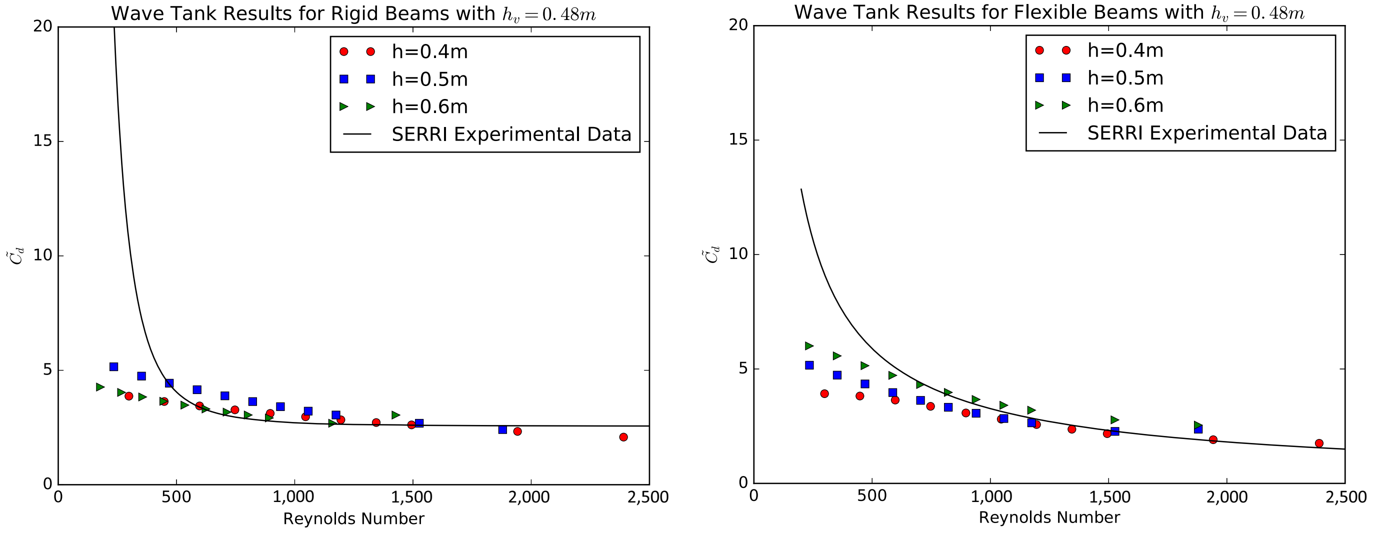

(a)

(b)

Fig. 3. Bulk drag coefficients for linear wave setups for (a) rigid; and (b) flexible beams compared to experimental results from the Southeast Region Research Initiative (SERRI).

- calculating the loads on beams [Eq. (19)] and momentum sinks [Eq. (17)] using velocities from t_{n-1} (the stem velocity can generally be ignored in the calculations because of its relative scale compared with the flow velocity);
- solving the beam systems for static states using the calculated loads and the solution from the previous time step as the initial guess for Newton's method, integrating to find $\boldsymbol{\chi}_k(t_n)$; and
- solving the fluid system [Eq. (1)] to time t_n.

This couples the dynamic fluid model and quasi-static structure model in a way that conserves momentum. The method has been validated for a variety of flow scenarios (Mattis et al. 2015).

Validation with Regular Waves

The numerical method was validated for a simple setup with regular linear plane waves and was compared to the experimental study by Wu et al. (2011). The experimental setup included a 20.6-m-long, 0.69-m-wide, 1.22-m-tall flat-bottomed wave flume. A paddle wave generator created regular waves on one end, and a porous, parabolic wave absorber was placed on the opposite end to minimize reflections. Between the lengths of 12.9 and 16.56 m, arrays of model vegetation were arranged in a staggered pattern. Wu et al. (2011) utilized several types of model *vegetation*, of which we focused on the two simplest. The first was a rigid vegetation type using wooden dowels with diameters of 9.4 mm and heights of 0.48 m. They were spaced with a population density of $N = 350$ stems/m^2. Second, their flexible vegetation consisted of ethylene propylene diene monomer (EPDM) foam-rubber cylinders, also with diameters of 9.4 mm and heights of 0.48 m. The spacing and density were the same as the rigid model as well. These foam hoses had a density of 368 kg/m^3 and Young's modulus of $E = 4$ MPa.

These setups were reproduced in the computational framework. For both types of model vegetation, simulations were run for three different mean water depths: 0.4, 0.5, and 0.6 m. This included one emergent-vegetation example, one submerged-vegetation example, and one example where the water depth was nearly the unbent vegetation height. Wavemaker boundary conditions were imposed to generate linear plane waves (Dalrymple et al. 1984). For each setup, the corresponding Reynolds numbers based on mean horizontal water velocity and bulk drag coefficients (C_D^{bulk}) were calculated in the way shown by Wu et al. (2011).

The calculated bulk drag coefficients using the immersed-structure method for specific Reynolds numbers for the three different depths and a curve fit for the experimental results are shown in Fig. 3. For very low Reynolds numbers, we underestimated the bulk drag. This was most likely because we were using $C_D^{\text{eff}} = 1.2$ for the drag coefficient of a single beam in the immersed-structure model. For Reynolds numbers this low, this is probably a smaller value of C_D^{eff} than what is realistic in nature, causing our method to result in a lower value for the drag coefficient. For a Reynolds number of approximately 500 and higher, our results matched the experimental results very closely. We captured the gradual decrease with respect to R that Wu et al. (2011) observed, with a similarly shaped dip. As with the experimental results, the bulk drag coefficient began to level off near Reynolds number 1,500. Above that, we calculated slightly lower values than the experiments, although there was a large spread to their data in that range. For these simple rigid and flexible setups with simple linear waves, bulk drag characteristics match extremely well with experimental data for moderate to large Reynolds numbers. Further details of this analysis can be found in the work by Mattis et al. (2012).

Computational Setup

Using the methods presented in the previous sections, we developed a computational model for the previously described wave flume. It would be computationally prohibitive to perform a full 3D simulation of the flume shown in Fig. 1. However, there are minimal 3D effects in the flow in the region before the vegetated region, and only a small amount of wave attenuation occurs in the prevegetation region. The fluid flow in the prevegetation region can be modeled adequately with a 2D (x-z) version of the two-phase flow method. We discretized the domain shown in Fig. 1 using a highly resolved unstructured triangular mesh with 376,591 elements with maximum diameters of $h_e = 0.02$ m. We added an absorbing condition on the sloped section behind the vegetation platform to minimize reflections. We did not include any vegetative obstacles in the simulation. We ran the two-phase flow model for wave series generated by each set of wave conditions from Table 2 for 400 s, with 30 backward Euler's time steps per peak wave period. The wave height and velocity profiles were recorded at each gauge (WG 1–13) for each time step. This 2D model accurately models the wave flume behavior without vegetation, as is shown in the next section.

We performed 3D simulations on a smaller section of the domain shown in Fig. 1. In the x-direction, we considered the flume starting at the beginning of the vegetation platform (WG 4) back to the sloping absorber. We considered the flume to be 0.4 m in the y-direction and 1 m deep (from the vegetation platform) in the z-direction. We discretized this 3D domain with approximately 1,000,000 unstructured tetrahedral elements with maximum diameters of $h_e = 0.035$ m. This mesh has been shown to have enough resolution to capture converged bulk flow characteristics (Mattis 2013). We took the wave heights and velocity profiles from the 2D simulations at WG 4 as Dirichlet's conditions to the 3D two-phase flow simulation, taking the same backward Euler's time steps as the 2D simulations. For the 3D simulations, we were able to include vegetative obstacles. In the vegetated region shown in Fig. 1, we placed vegetative obstacles arranged as shown in Fig. 2 in the x,y-plane for cases of $N = 200$ and 400 stems/m^2, totaling 784 and 1,568 vegetative obstacles, respectively. The simulations were run with the immersed-structure method to model the interaction between the flow and vegetative obstacles. In the structure model for the vegetative obstacles, five quadratic elements were used for each obstacle, which follows a common rule-of-thumb for ratios of Eulerian and Lagrangian mesh resolutions for immersed-boundary methods. Young's modulus, length, density, and diameter of the obstacles were considered to be the same as the XLPO tubing used in the experiments. As with the 2D simulations, we imposed an absorbing condition on the sloped section behind the vegetation platform. Fig. 4 shows the deflections of a section of vegetative obstacles as a wave passes through, showing the robustness of the method for capturing large deflections. Measurements of wave heights were taken at WGs 5–13 at each time step. We used these wave-height measurements to analyze wave attenuation due to the vegetation and compare to experimental results from Anderson and Smith (2014).

Analysis

Wave attenuation can be analyzed in a variety of ways. Attenuation affects the wave heights, wave spectra, and wave energies. Using wave-height data from computational experiments, we analyzed these effects and compared them to values calculated from experimental data. It should be noted that, for such complex systems, it is often impossible or infeasible to exactly reproduce values calculated with different experimental setups or evaluation methods because of measurement error, the effect of spatial and temporal averaging, and nonlinear effects. A good way to compare results from different methods is to see if their trends with respect to essential parameters are the same and if fitted results based on accepted models exhibit similar behavior.

Wave-Height Attenuation Analysis

The effects of stem density, submergence ratio, incident wave height, and peak wave period on wave height are of much interest to those who study coastal wave attenuation. Using the detrended free surface elevation information at the WGs, the wave spectral density [$S(f)$] was calculated at each gauge using a fast Fourier transformation. At each gauge, a cubic spline of the outputted wave elevations was constructed and sampled at 8,000 equal times. These samples were used to calculate the spectra. The spectra were smoothed using a boxcar filter over five neighboring frequency bands. The spectra were cut off above the frequency of 2 Hz, resulting in n frequency components with a resolution of Δf.

Fig. 5 shows calculated wave spectral densities for the computational wave flume [Fig. 5(a)] and the experimental wave flume [Fig. 5(b)] at five different gauges (WG 1, WG 5, WG 7, WG 10, and WG 13) for the control case with $N = 0\,\mathrm{stems/m^2}$ for Run number 13 with $l_v/h = 1.36$, $H_0/h = 0.37$, and $h/L_p = 0.11$. The structures of the spectra were quite similar, with peaks at a peak frequency of $f = 0.67$ Hz and a thicker tail in the higher-frequency region, which is seen in the TMA spectrum. Also, a small peak at approximately $f = 1.2$ Hz appeared in both cases. This peak, as noted by Anderson and Smith (2014), was due to nonlinear wave interaction and shoaling moving down the flume and up the ramp. The computational results for wave density were systematically 10–20% smaller than the experimental results, possibly due to the numerical wave generation and some numerical dissipation on the ramp. The computational results also showed a slight energy loss between WGs 5 and 7, where the experimental results showed only a very small change. A small amount of spectral attenuation was seen at all frequencies as the waves traveled farther down the flume due to bottom friction and other damping effects. Figs. 6 and 7 show spectra for the same wave setups with vegetation included, with $N = 200$ and $400\,\mathrm{stems/m^2}$, respectively. As with the control case, the structures of the spectra were similar; however, the computational results generally exhibited more dissipation. Note that these cases exhibited more dissipation between WG 1 and WG 5 (the region before the vegetation) than the control case. This dissipation may have arose from a variety of factors, including the coarser mesh resolution of the 3D model and increased subgrid scale turbulence effects. The small peak at approximately 1.2 Hz persisted as well. In the case with $N = 200\,\mathrm{stems/m^2}$, a greater loss of wave energy was seen than for the control at all frequencies, as one would expect. In the case with $N = 400\,\mathrm{stems/m^2}$, there was greater loss of wave energy than with $N = 200\,\mathrm{stems/m^2}$. Similar differences were seen in the computational wave flume and experimental results. These results showed that the method of fluid–vegetation interaction used in the computational wave flume, which has previously been used to accurately predict values, such as form drag, had the predicted effect on the attenuation of waves.

The wave spectral density can be used to calculate the zero-moment wave height (H) by

$$H = 4\sqrt{\sum_{j=1}^{n} S(f)_j \Delta f} \tag{20}$$

Given M distinct waves, the root-mean-square wave height (H_{rms}) is calculated by individual wave heights (H_j) by

$$H_{\mathrm{rms}} = \sqrt{\frac{1}{M}\sum_{j=1}^{M} H_j^2} \tag{21}$$

The incident wave height (H_0) was taken as the zero-moment wave height at the leading edge of the vegetation (WG 5). Wave-height attenuation is generally quantified with an exponential decay function

$$\frac{H}{H_0} = \exp\left(-k_i x\right) \tag{22}$$

where k_i = wave-decay coefficient; and x = horizontal distance from the leading edge of the vegetation. For each setup, k_i was

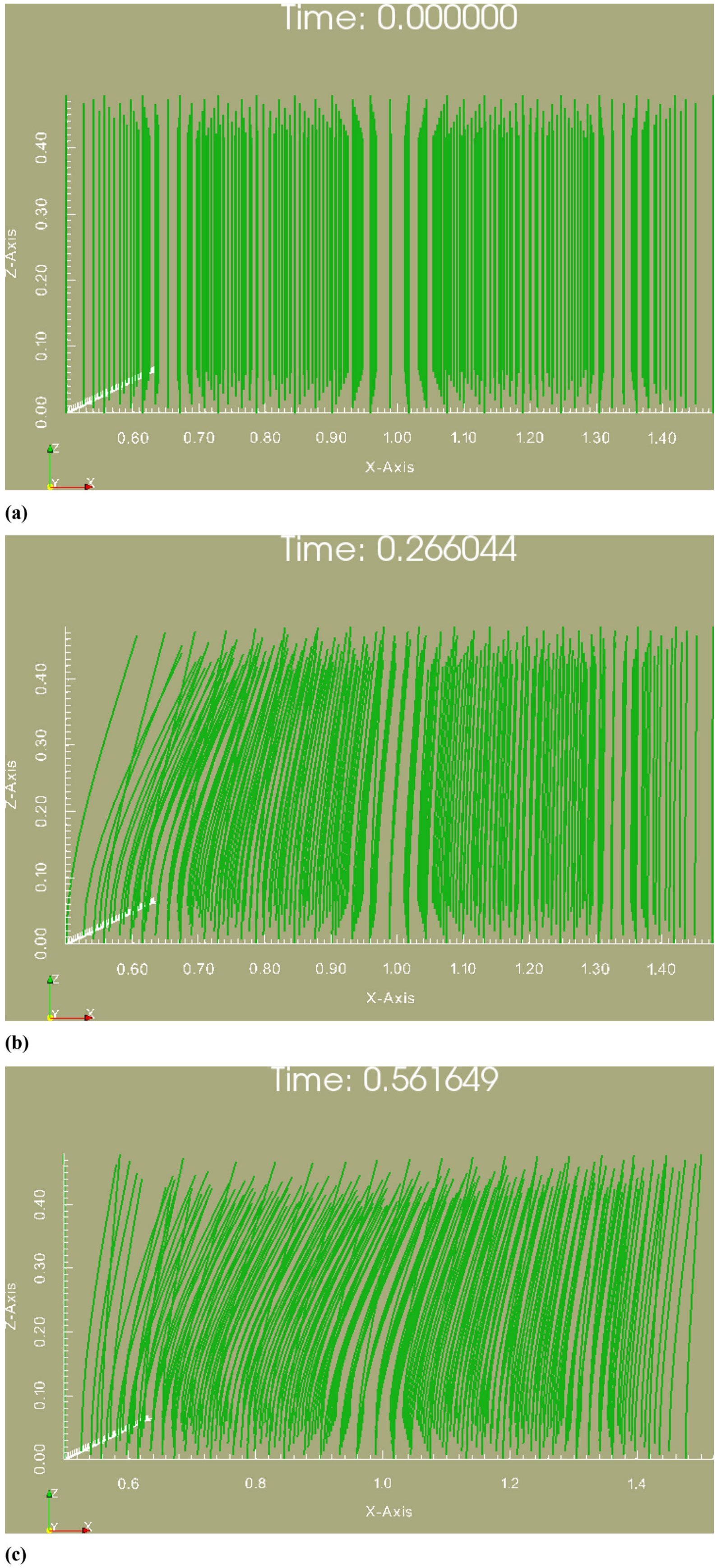

Fig. 4. Wave traveling through a bed of model flexible vegetation at times (a) 0.0 s; (b) 0.27 s; (c) 0.56 s; (d) 0.86 s; (e) 1.15 s; and (f) 1.45 s.

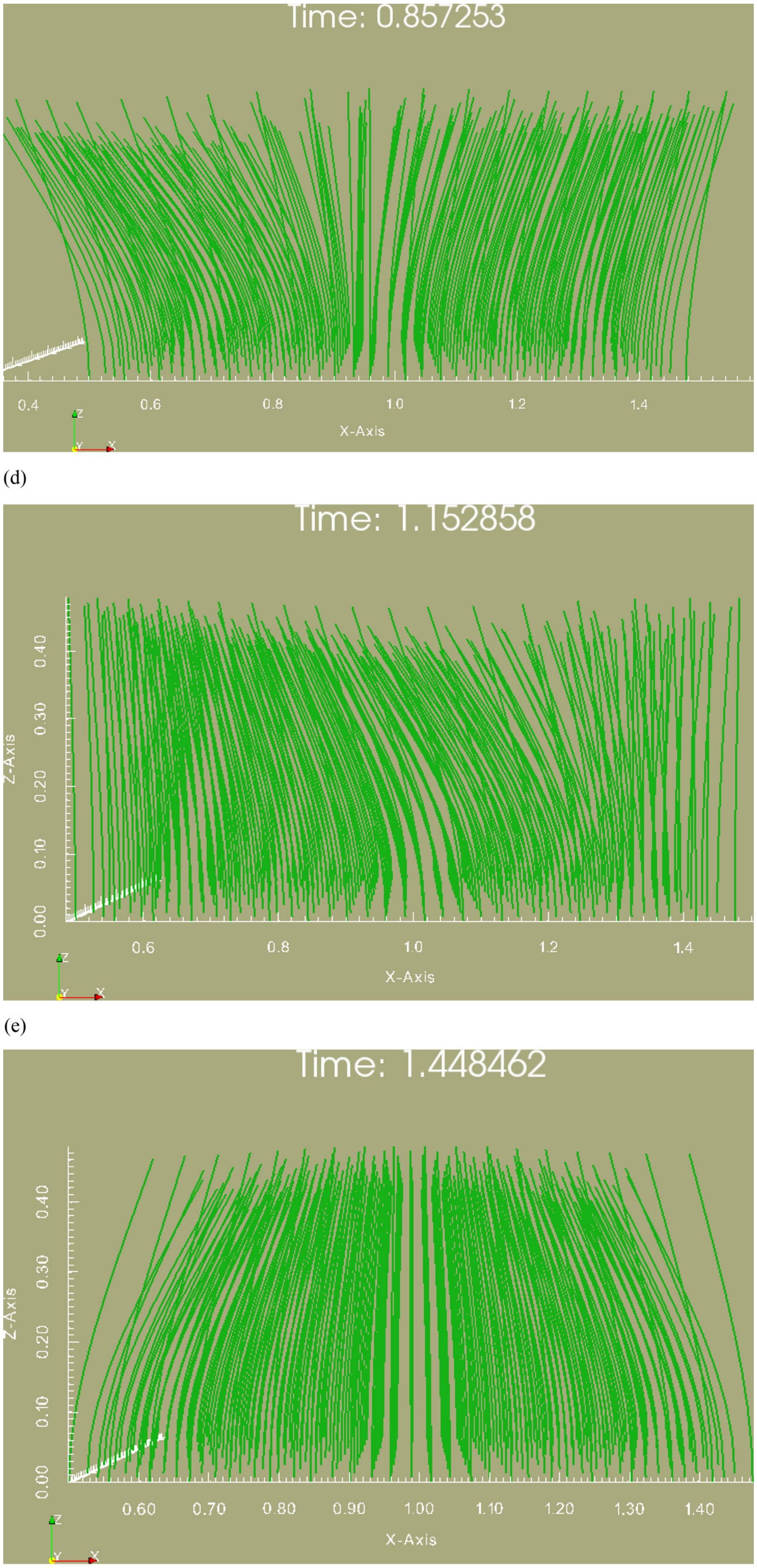

(d)

(e)

(f)

Fig. 4. (*Continued.*)

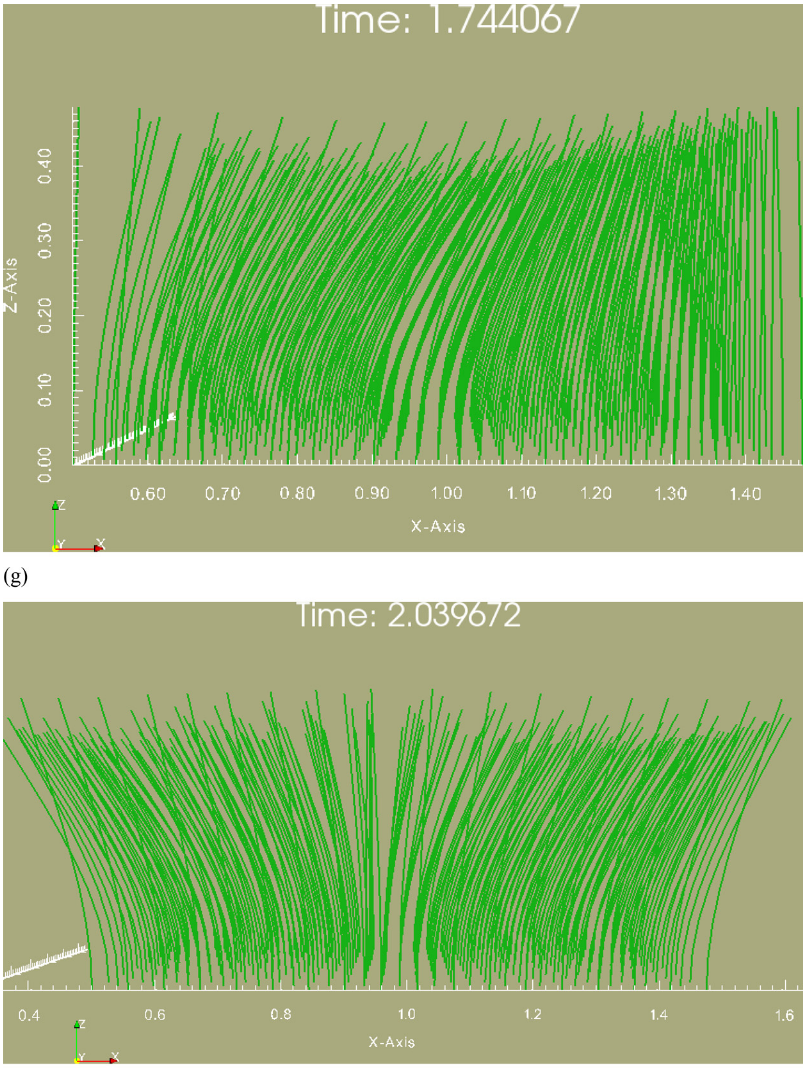

(g)

(h)

Fig. 4. (*Continued.*)

calculated using a Gauss-Newton nonlinear least-squares fit using data from WGs 6–13. Over these setups, the root-mean-square error (RMSE) between computational and experimental calculations of k_i was 0.0095 for $N = 200\,\mathrm{stems/m^2}$ and 0.025 for $N = 400\,\mathrm{stems/m^2}$.

There are a few dimensionless parameters for which it is valuable to study trends in the wave-decay coefficient. One of these dimensionless parameters is the stem-submergence ratio (l_v/h). When $l_v/h < 1$, it is in the regime of submerged vegetation: the water level is above the top of the vegetation. When $l_v/h > 1$, it is in the regime of emergent vegetation. Fig. 8 shows the effect of the submergence ratio on cases where other parameters ($H_0 = 0.11$ m and $T_p = 1.5$ s) were kept constant, as in the published analysis of the experimental data (Anderson and Smith 2014). Results from the computational wave flume are shown in Fig. 8(a). The results from the experiments are shown in Fig. 8(b). For the control cases, the decay coefficient was a small value close to zero, because little attenuation occurred. For the cases of $N = 200$ and $400\,\mathrm{stems/m^2}$, there was a tendency for k_i to increase (nearly linearly) at a high rate with the submergence ratio. Therefore, having more of the vertical profile containing vegetation increased the amount of decay. The stem density (N) had a significant effect on k_i, with the higher-density cases having much higher values of k_i. The same trends were shown with the computational and experimental results with a small variation in the magnitudes of values. The rate of wave decay increased with higher vegetation densities and submergence ratios.

Another dimensionless parameter of interest is the relative wave height (H_0/h), the ratio of the incident wave height to the mean water depth. This was used to study the effects of incident wave heights. Fig. 9 shows the effect of relative wave height on cases where the relative depth was $h/L_p = 0.17$ (open symbols) or 0.12 (closed symbols). Results from the computational wave flume are shown in Fig. 9(a). Results from the experiments are shown in Fig. 9(b). For the control case with no vegetation, there was only a small amount of wave decay. In all cases, there was a clear trend that wave decay increased slightly with relative wave height. This trend is explainable because bottom effects more greatly affect higher waves. For the experimental results, there was a clear linear trend, whereas with the computational results there were overall linear trends with similar magnitudes as the experimental results, with slight pollution from numerical error. In both the computational and experimental results for these cases, the relative depth (h/L_p) had no apparent effect on attenuation. As was expected, the stem density had a major influence on wave decay, with much more decay with higher stem densities. There was an overall trend where the rate of

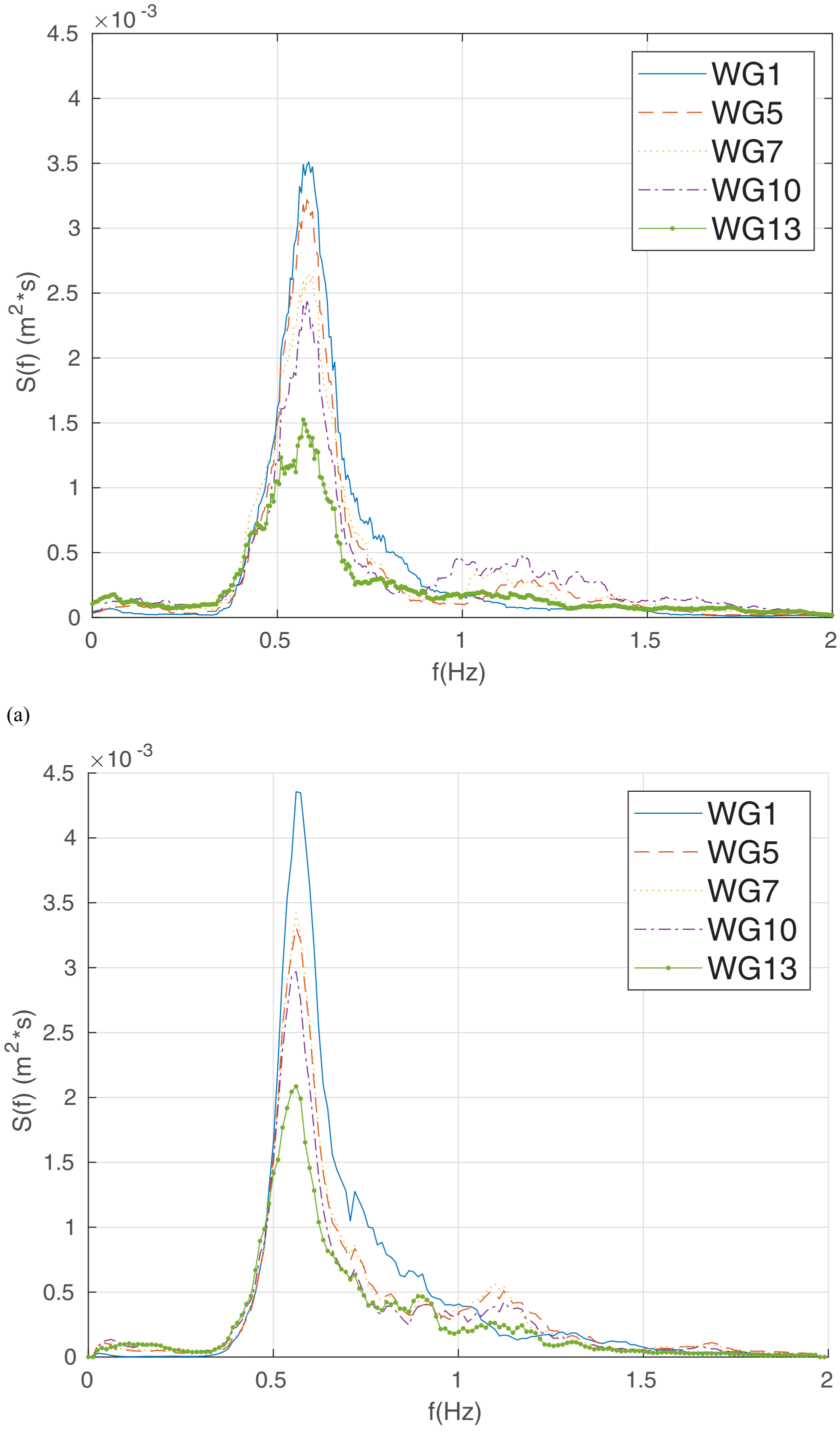

(a)

(b)

Fig. 5. Wave spectral density for Run number 13 with $l_v/h = 1.36$, $H_0/h = 0.37$, $h/L_p = 0.11$, and no vegetation ($N = 0\,\text{stems/m}^2$) from (a) computational wave flume; and (b) experiments.

wave decay increased with higher vegetation densities and relative wave heights.

The relative depth (h/L_p) is another dimensionless parameter of interest. This was used to study the effects of peak period. Fig. 10 shows the effect of relative depth on cases where the submergence ratio was $l_v/h = 1.36$ (open symbols) or 0.78 (closed symbols). The results from the computational wave flume are shown in Fig. 10(a). The results from the experiments are shown in Fig. 10(b). In both the experimental and computational results, relative depth had very little impact on the rate of wave decay. There was some variation between the computational and experimental results, but both showed no trends. Relative depth had little influence on the wave-decay rate.

Spectral-Attenuation Analysis

Wave energy has been shown to be dissipated at different rates and at different frequency components. The dissipation (change in wave

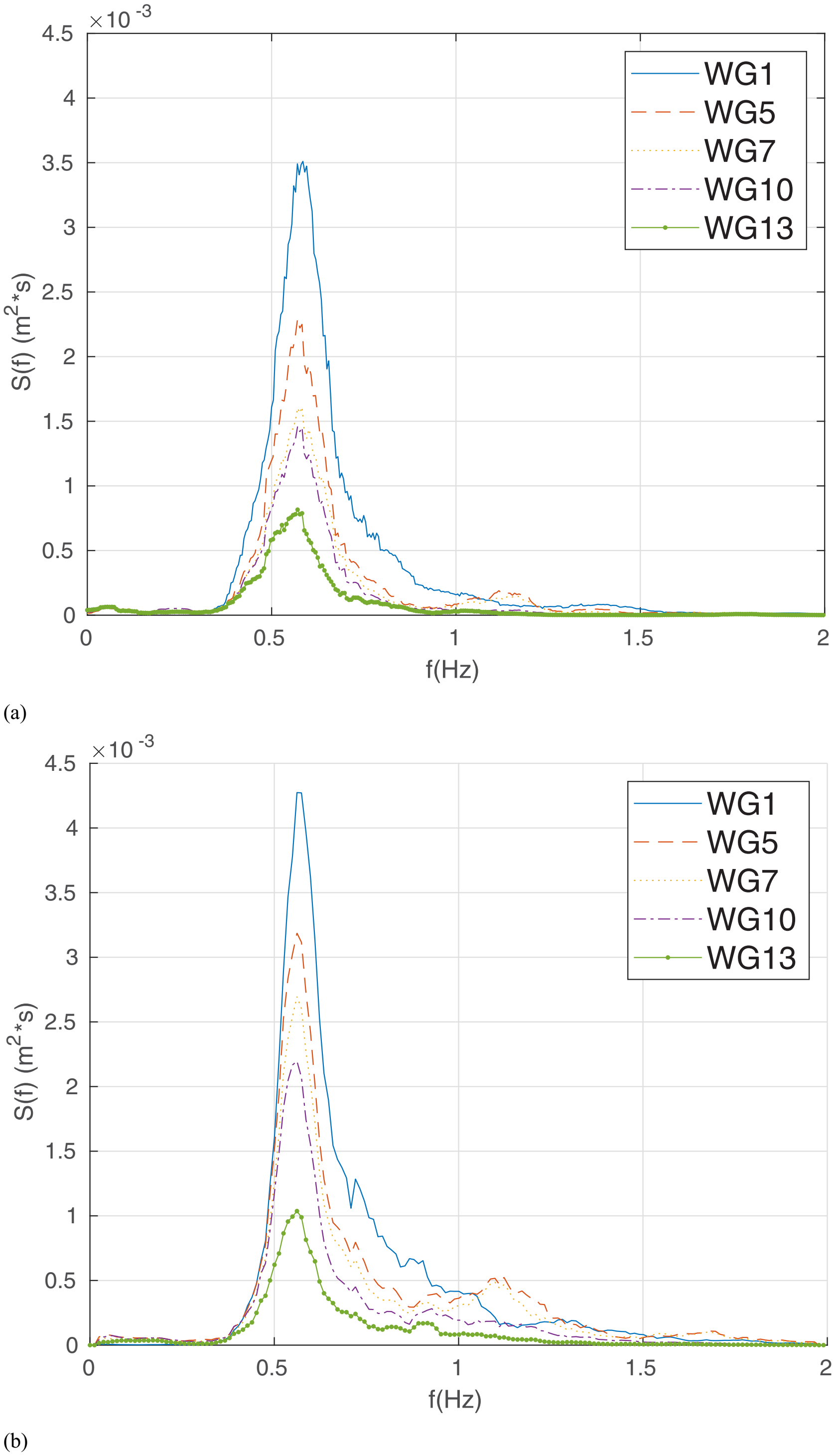

Fig. 6. Wave spectral density for Run number 13 with $l_v/h = 1.36$, $H_0/h = 0.37$, $h/L_p = 0.11$, and $N = 200\,\mathrm{stems/m^2}$ from (a) computational wave flume; and (b) experiments.

energy, ϵ) at each frequency component (j) as a function of the initial energy is described by the energy-flux equation

$$\frac{\Delta E_j}{E_j} = \epsilon \tag{23}$$

where E_j = component wave-energy density. Assuming linear waves, the component wave-energy density is defined by

$$E_j = \frac{1}{2}\rho g a_j^2 \tag{24}$$

where ρ = water density; g = gravitational constant; and a_j = component wave amplitude defined by $a_j = \sqrt{2S(f)_j \Delta f}$.

The energy dissipation was calculated between WGs 5–7 and WGs 5–13 located in the vegetated region. Fig. 11 shows these calculations for Run 14 with $l_v/h = 1.36$, $H_0/h = 0.36$, $h/L_p = 0.09$, and a high stem density of $N = 400\,\mathrm{stems/m^2}$. The log-scale spectra for the computational [Fig. 11(a)] and experimental [Fig. 11(b)] setups are shown for different locations in the

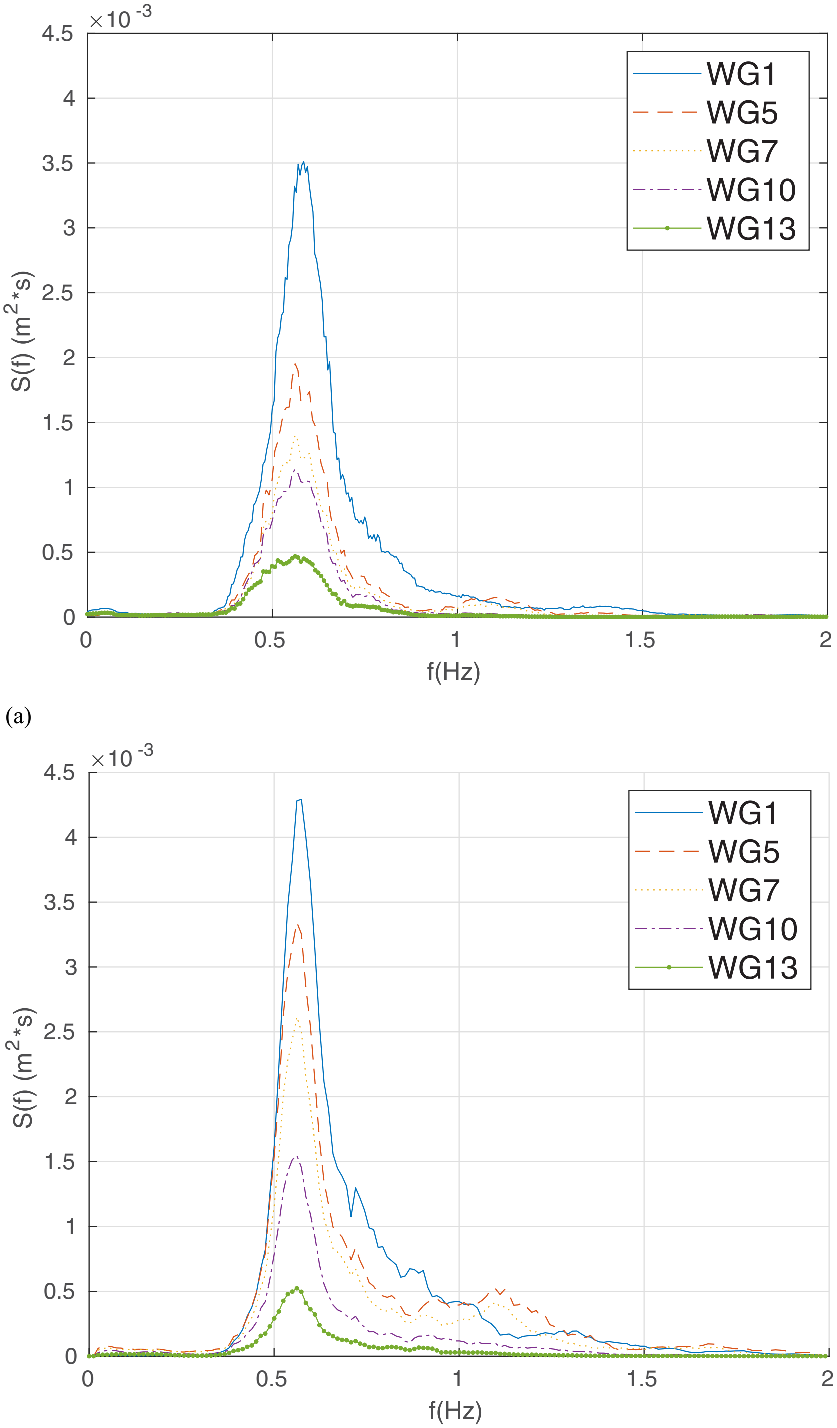

(a)

(b)

Fig. 7. Wave spectral density for Run number 13 with $l_v/h = 1.36$, $H_0/h = 0.37$, $h/L_p = 0.11$, and $N = 400\,\mathrm{stems/m^2}$ from (a) computational wave flume; and (b) experiments.

vegetated domain at WG 5, WG 7, WG 10, and WG 13. As discussed earlier, the structures of the spectra from computations and experiments were quite similar. The normalized energy loss (ϵ) is shown for the computational [Fig. 11(c)] and experimental setups [Fig. 11(d)]. The dissipation rate fluctuated considerably with frequency in both the computational and experimental results. For both cases, there were noticeable peaks in dissipation near $f = 1$ and 1.5 Hz. Anderson and Smith (2014) proposed that these exist due to energy exchange between wave harmonics. In both cases, the general trend of the dissipation rate being higher at higher frequencies was seen. For the dissipation calculated between WG 5 and WG 13, the dissipation had mostly stabilized for much of the frequency range. The tendency of higher rates of dissipation for higher frequency components has also been realized in field experiments (Bradley and Houser 2009; Lowe et al. 2007). Many of the qualitative characteristics of the wave-energy spectra and dissipation rates were the same in the experiments and computational results.

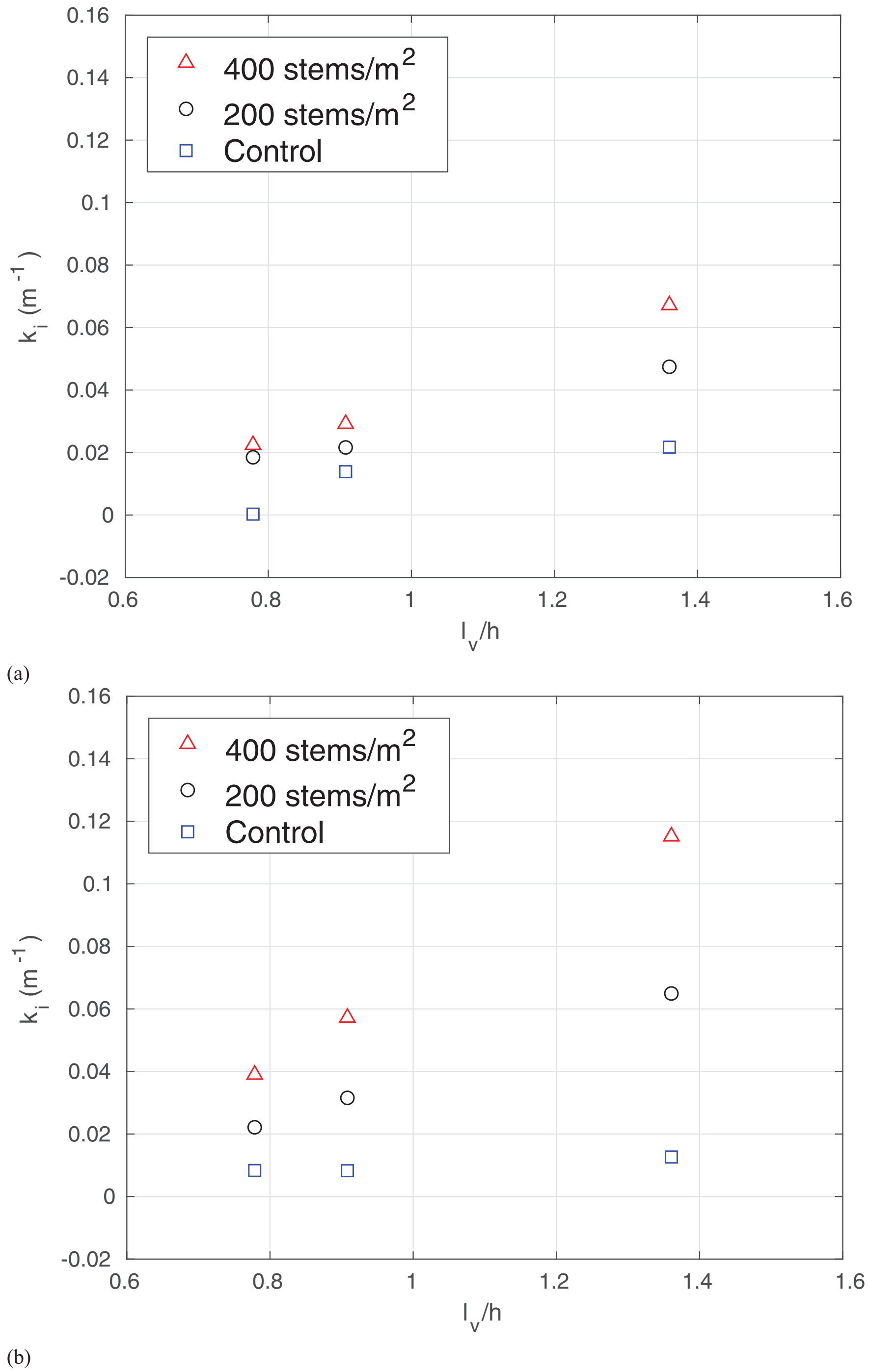

Fig. 8. Effect of stem-submergence ratio (l_v/h) on wave-decay coefficient (k_i) for $H_0 = 0.11$ s and $T_p = 1.5$ s for (a) computational wave flume; and (b) experiments.

Energy-Attenuation Analysis

We quantified wave-energy dissipation in the manner done by Anderson and Smith (2014). According to Dalrymple et al. (1984), using the conservation of the energy-flux equation, the energy dissipation (S_v) is defined by

$$S_v = \int_{-h}^{-h+l_v} F_x u dz = \int_{-h}^{-h+\alpha h} \frac{1}{2} \rho C_D b_v N u|u| dz \tag{25}$$

where F_x = horizontal drag force; u = horizontal velocity of the wave; C_D = depth-averaged bulk drag coefficient; and ρ = fluid density. Note that the bulk drag coefficient generally does depend on Reynolds number, stem arrangement, and other factors for such flow scenarios, whereas the cross-sectional geometry-based local drag coefficient for a single stem (C_D^{eff}) can be assumed to be constant for the range of Reynolds numbers usually encountered in coastal flows. Applying linear wave theory, Eq. (25) can be expressed as

$$S_v = \frac{2}{3\pi} \rho C_D N b_v \left(\frac{gk}{\omega}\right) \frac{\sinh^3 k\alpha h + 3\sinh k\alpha h}{3k \cosh^3 kh} A^3 \tag{26}$$

J. Waterway, Port, Coastal, Ocean Eng., 2019, 145(1): 04018033

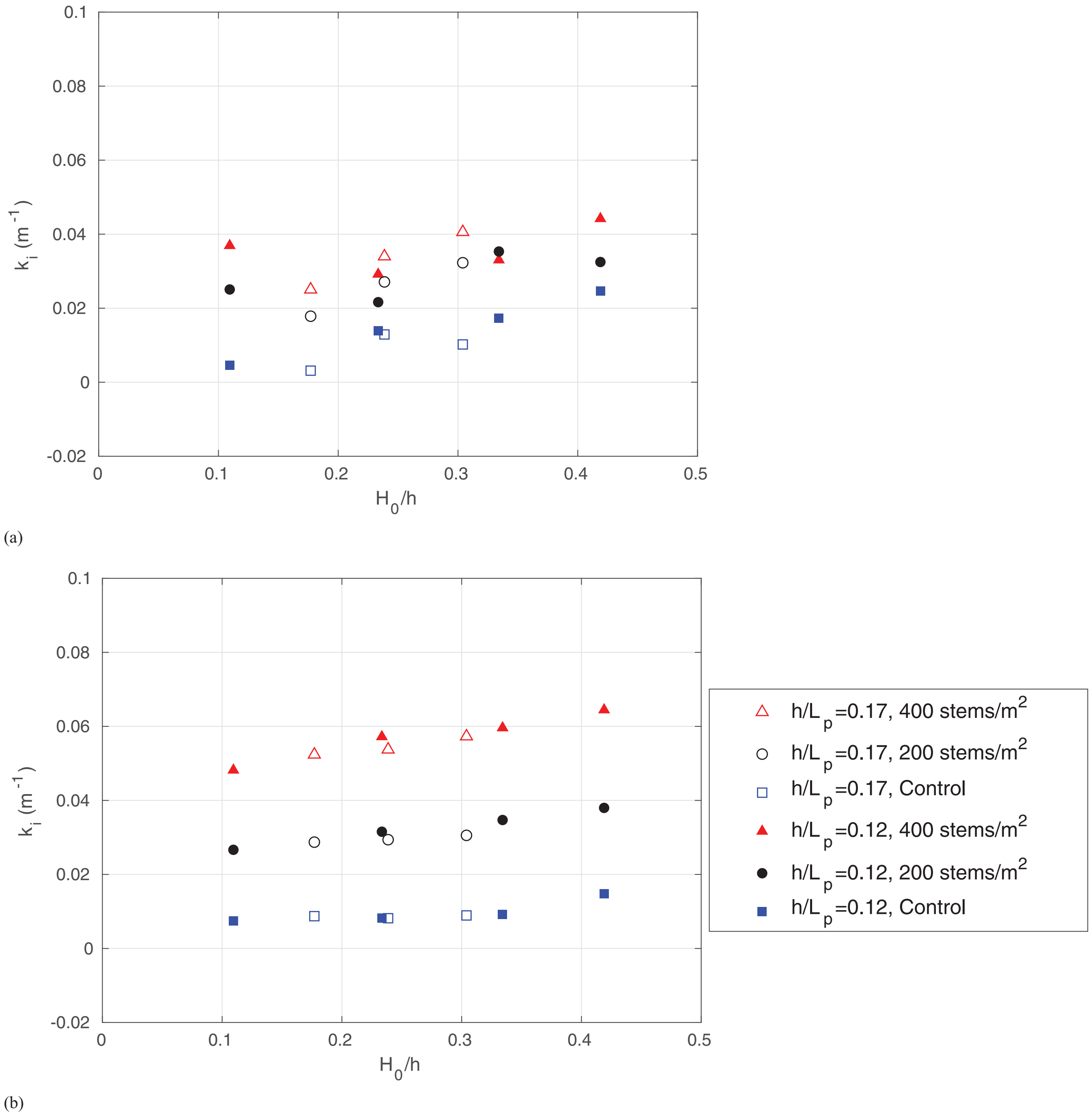

Fig. 9. Effect of relative wave height (H_0/h) on wave-decay coefficient (k_i) for l_v/h = 0.91 for (a) computational wave flume; and (b) experiments.

where k = angular wave number; ω = angular frequency; A = wave amplitude; and $\alpha = l_v/h$ for submerged vegetation and $\alpha = 1$ for emergent vegetation. Mendez and Losada (2004) expanded on this formulation, assuming an unmodified Raleigh's distribution and described wave-height evolution for nonbreaking random waves over constant depth as

$$\frac{H_{\mathrm{rms}}}{H_{\mathrm{rms},0}} = \frac{1}{1+\beta x} \tag{27}$$

where $H_{\mathrm{rms},0}$ = incident root-mean-square wave height; x = distance from the beginning of the vegetation; and

$$\beta = \frac{1}{3\sqrt{\pi}} C_D N b_v k \frac{\sinh^3 k\alpha h + 3\sinh k\alpha h}{(\sinh 2kh + 2kh)\sinh kh} H_{\mathrm{rms},0} \tag{28}$$

Plugging Eq. (28) into Eq. (27), we have a nonlinear equation where all values are known, except for C_D. We performed a nonlinear least-squares fit using the Gauss-Newton method using data at all of the gauges located within the vegetation (WGs 6–13) to calculate C_D for all model setups. This value is associated with the magnitude of energy dissipation.

As seen previously, it is useful to study the trend of C_D with respect to certain dimensionless parameters. It has been shown that bulk drag coefficients exhibit interesting behavior with respect to

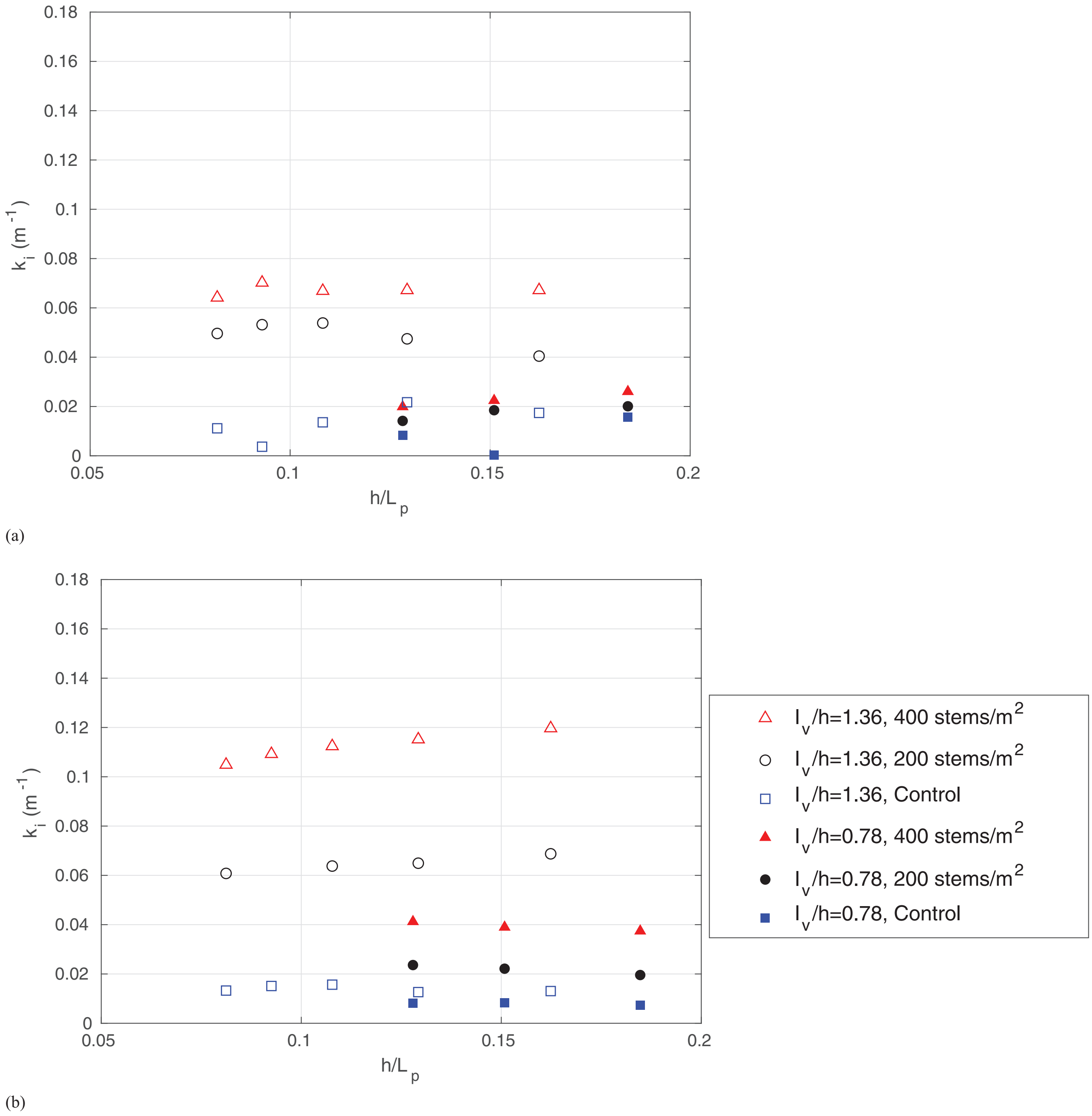

Fig. 10. Effect of relative depth (h/L_p) on wave-decay coefficient (k_i) for (a) computational wave flume; and (b) experiments.

dimensionless measures of velocity (Mattis et al. 2012, 2015). One of these is the stem Reynolds number, defined as

$$\mathsf{R} = \frac{u_c b_v}{\nu} \tag{29}$$

where ν = kinematic viscosity of water; and u_c = characteristic velocity acting on a stem. As done by Anderson and Smith (2014), the characteristic velocity was taken as the maximum horizontal velocity at the beginning of the vegetated region (WG 5) at the top of the vegetation, which can be approximated by

$$u_c = \frac{H_{\mathrm{rms}}}{2}\omega_p\left(\frac{\cosh k\alpha h}{\sinh kh}\right) \tag{30}$$

where ω_p = peak angular frequency of the wave series. Another useful nondimensionalization of velocity is with the Keulegan-Carpenter number, defined by

$$\mathrm{KC} = \frac{u_c T_p}{b_v} \tag{31}$$

Kobayashi et al. (1993) presented an empirical relationship between C_D and these dimensionless parameters

$$C_D = B + \left(\frac{\kappa}{\mathsf{R}}\right)^c \tag{32}$$

$$C_D = B + \left(\frac{\kappa}{\mathrm{KC}}\right)^c \tag{33}$$

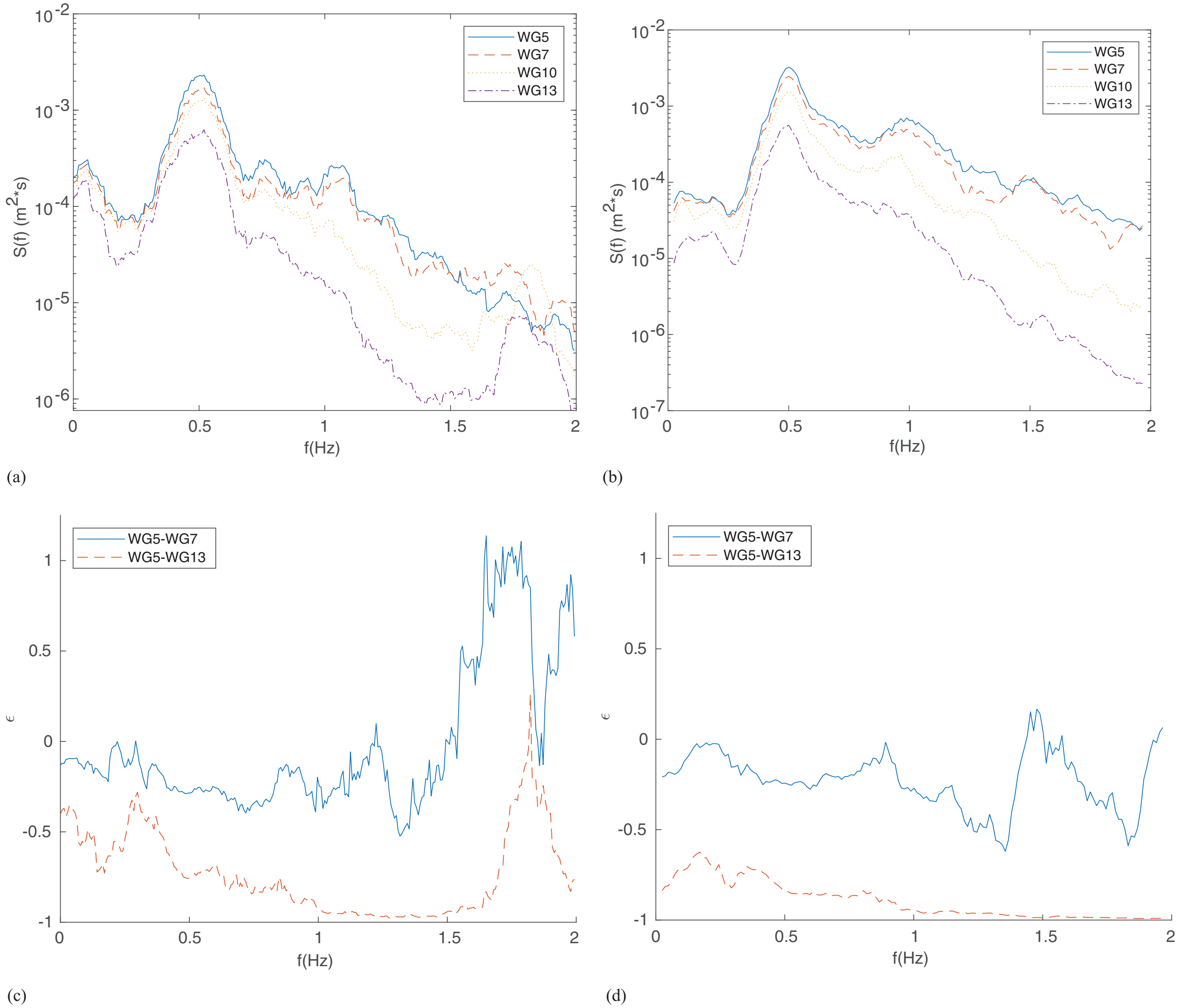

(a) (b) (c) (d)

Fig. 11. (a and b) Band-averaged wave spectral density [$S(f)$]; and (c and d) normalized energy loss (ϵ) for Run 14 with $l_v/h = 1.36$, $H_0/h = 0.36$, $h/L_p = 0.09$, and high stem density $N = 400\ \mathrm{stems/m^2}$. Plots (a) and (c) show computational wave flume results, and plots (b) and (d) show experimental results.

As was done by Anderson and Smith (2014), we calculated least-squares fits for (B, κ, c) using the calculated drag coefficients. These fits did well for the case of submerged vegetation ($l_v < h$) but not for emergent vegetation ($l_v > h$), as was seen in other work. The drag coefficients tended to be higher for emergent cases. Therefore, for these fits, we only used the data from submerged vegetation. Over the entire collection of wave setups, RMSE between drag coefficients was 0.309 for $N = 200$ stems/m^2 and 0.366 for $N = 400$ stems/m^2.

Fig. 12 shows the effect of Reynolds number on drag coefficient with C_D calculated from the computational wave tank [Fig. 12(a)] and the experiments [Fig. 12(b)]. For the computational results, values of (B, κ, c) of (1.15, 552.0, 3.79) were calculated, and from the experiments, the values were (0.76, 744.2, 1.27), as shown in Figs. 12(a and b). In both cases, we see that the cases of emergent vegetation resulted in higher drag coefficients. The trend that was most noticeable was that C_D decreased with Reynolds number before leveling off. This is a well-known tendency of drag coefficients. There was a great deal more spread in the results calculated from the computational wave flume than from the experiments, but the least-squares fits were quite similar. The least-squares fit from the computational results had $r^2 = 0.378$, and the computational data compared to the experimental fit had $r^2 = 0.231$. However, the RMSE between the two regressions was only 0.160. The least-squares fit of Fig. 13 shows similar results with respect to the Keulegan-Carpenter number. The values of (B, κ, c) were (1.15, 25.7, 5.27) for the computational results and (1.10, 27.4, 3.08) for the experimental results. Similar to R, the results from the computational tank had more spread, but the fitting curves were very similar. C_D was also seen to decrease with KC before leveling off. The least-squares fit from the computational results had $r^2 = 0.392$, and the computational data compared to the experimental fit had $r^2 = 0.301$. The RMSE between the two regressions was 0.128.

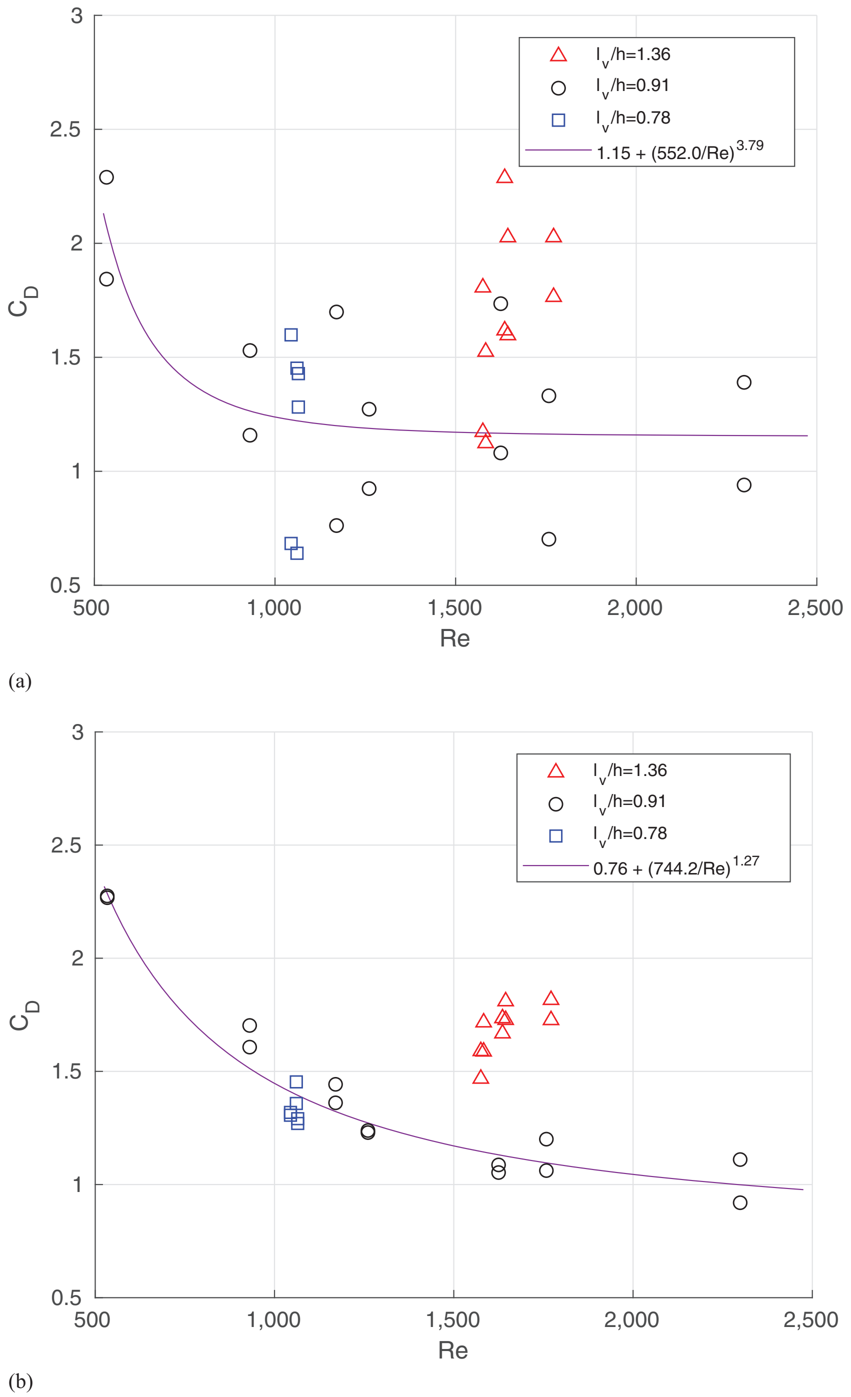

Fig. 12. Effect of Reynolds number on drag coefficient (C_D) for (a) computational wave flume; and (b) experiments. Different symbols represent different values of l_v/h.

Mendez and Losada (2004) used modified versions of R and KC to better handle cases of emergent vegetation. They defined the modified Reynolds number as $Q_{\mathsf{R}} = \mathsf{R}(l_v/h)^{-1.5}$ and modified Keulegan-Carpenter number as $Q_{\mathrm{KC}} = \mathrm{KC}(l_v/h)^{-1.5}$. Variations of Eqs. (32) and (33) can be obtained by replacing R with Q_{R} and replacing KC with Q_{KC}. Again, the values B, κ, and c were calculated using a nonlinear least-squares fit; however, the emergent cases were included. Fig. 14 shows the effect of modified Reynolds number on drag coefficient with C_D calculated from the computational wave tank [Fig. 14(a)] and the experiments [Fig. 14(b)], along with the fitted curve. In both cases, the modified model much better modeled the behavior of emergent vegetation (triangles). From the computational tank, (B, κ, c) was calculated as (0.64, 952.8, 0.92) and was (0.11, 2067.7, 0.64) from the experiments. Similar to the unmodified model, the computational results had a greater spread, but the fitted curves were close to each other. The least-squares fit from the computational results had $r^2 = 0.329$, and the computational data compared to the experimental fit had $r^2 = 0.297$. The RMSE between the two regressions was only 0.079. Fig. 15 shows the effect of modified Keulegan-Carpenter number on drag coefficient with C_D calculated from the computational wave tank [Fig. 15(a)] and the

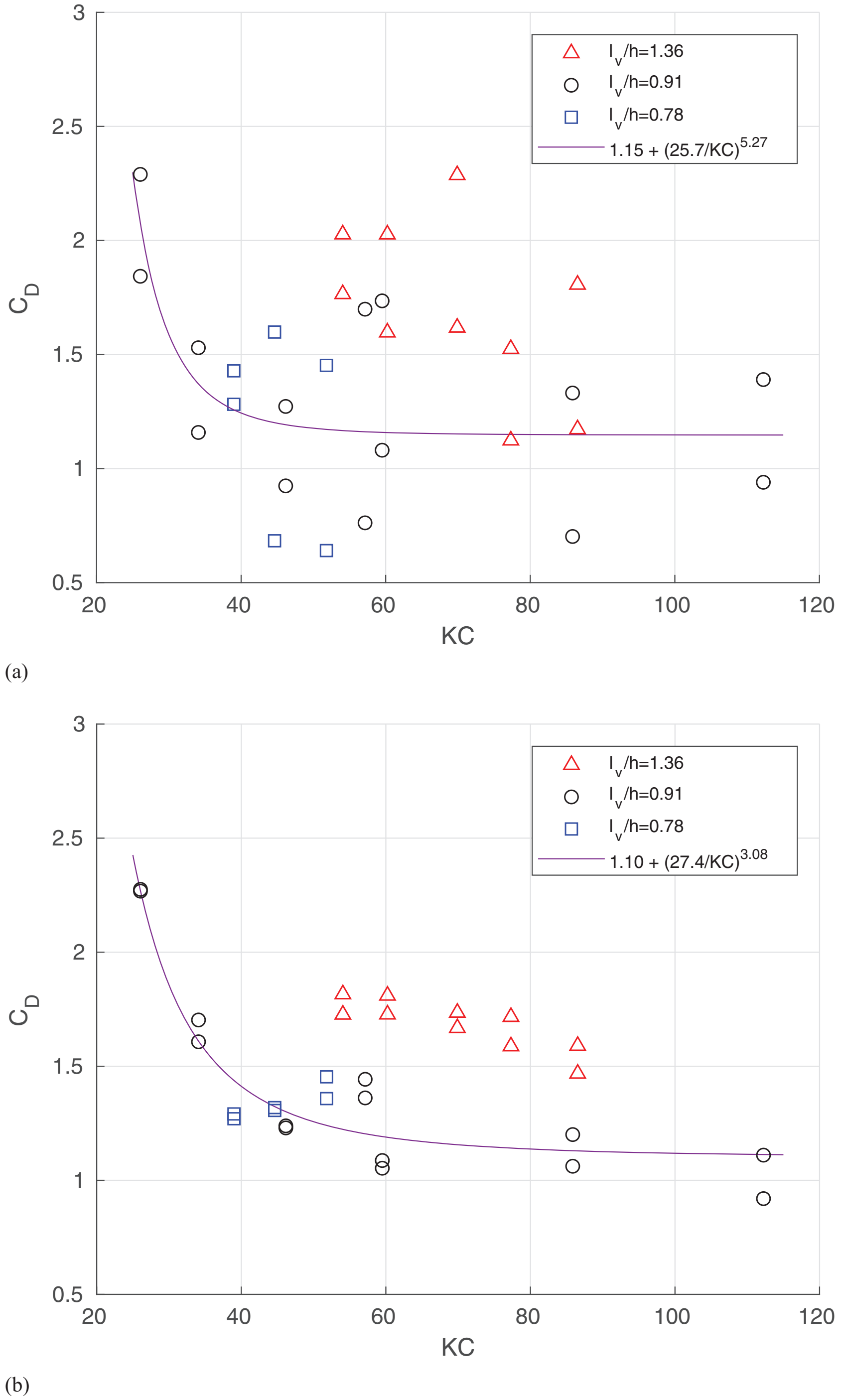

Fig. 13. Effect of Keulegan-Carpenter number on drag coefficient (C_D) for (a) computational wave flume; and (b) experiments. Different symbols represent different values of l_v/h.

experiments [Fig. 15(b)], along with the fitted curve. In both cases, the modified model much better modeled the behavior of emergent vegetation (triangles). From the computational tank, (B, κ, c) was calculated as (0.97, 32.2, 1.84) and as (0.97, 33.5, 1.69) from the experiments. These parameters resulted in almost identical curves. It is shown that, with respect to all of the dimensionless velocity terms (R, KC, Q_{R}, and Q_{KC}), there was greater variance in the results calculated using the computational wave flume; however, the fitted models from both were extremely similar to each other. The least-squares fit from the computational results had $r^2 = 0.410$, and the computational data compared to the experimental fit had $r^2 = 0.394$. The RMSE between the two regressions was 0.056.

There were large variances in the drag coefficient data from the computational setups compared to those from the experimental results. These large variances led to relatively poor r^2 scores in the fit of drag laws to the data. The large variances were likely due to combinations of sources of error in the calculations of C_D, including numerical error from solving the model and the many steps of post-processing for the model output. Errors may also come from modeling assumptions regarding the idealized vegetation, the local drag relation, and the ignoring of stem–stem interactions. In particular,

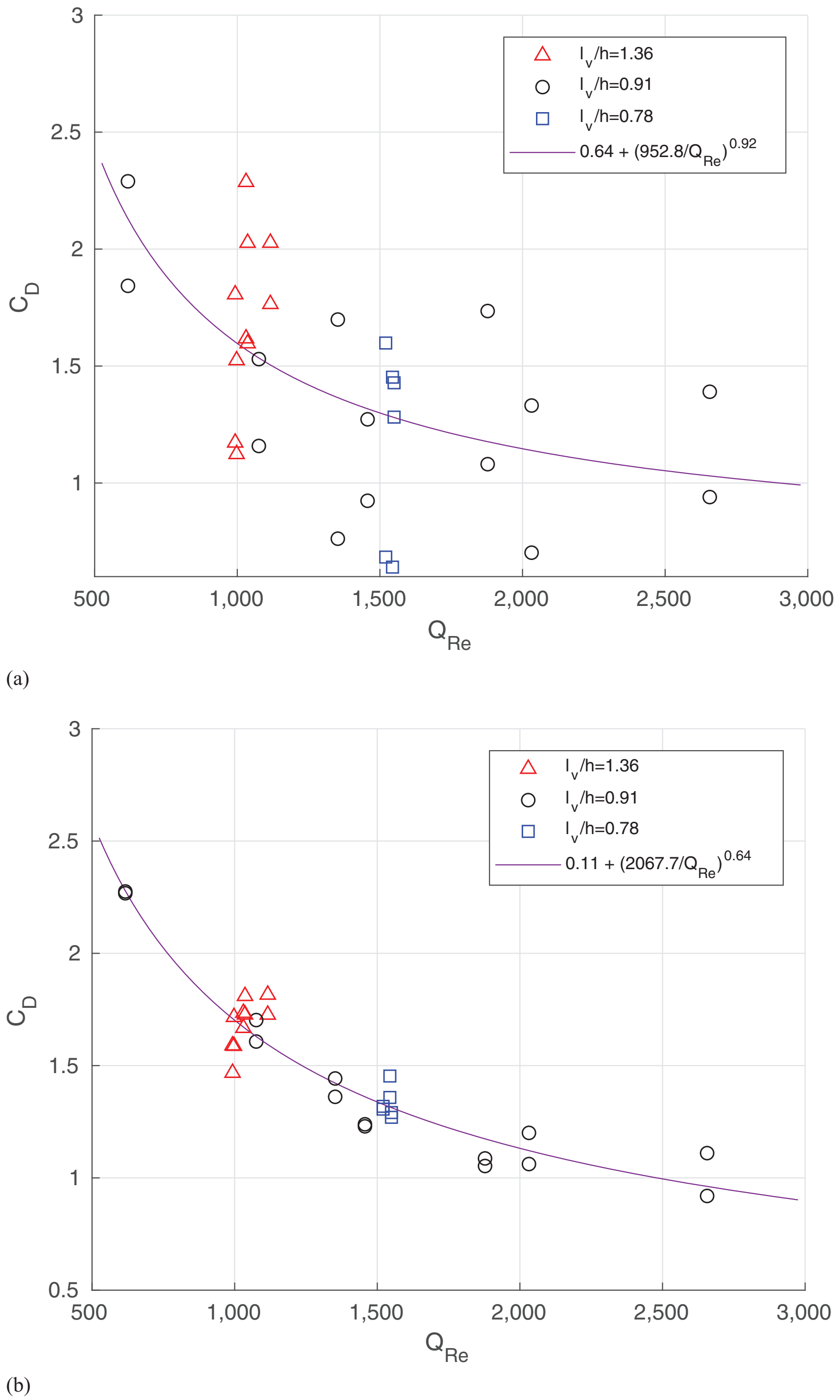

Fig. 14. Effect of modified Reynolds number on drag coefficient (C_D) for (a) computational wave flume; and (b) experiments. Different symbols represent different values of l_v/h.

the better fits to experimental data in the validation study with regular waves for rigid and semiflexible obstacles where there is little or no stem–stem interaction than with irregular waves and more flexible obstacles could indicate that ignoring stem–stem interaction introduces some modeling error. However, the regressions calculated according to the drag laws fit the experimental data nearly as well as the computational data, and the RMSE between the two regressions tended to be relatively small. This suggests that the effect of the combinations of sources of numerical error was similar to a large amount of noise polluting the data. The individual data points were noisy, but the overall trend matched the experiments much better. In future work, we hope to see this effect reduced by numerical refinement in solving the model and postprocessing.

Conclusions

In this paper, we presented a model for a computational wave flume containing vegetation that requires a minimal number of modeling assumptions. The model coupled a two-phase flow model and a model for thin-elastic structures via an immersed-structure method. The mathematical model was implemented with the open-source

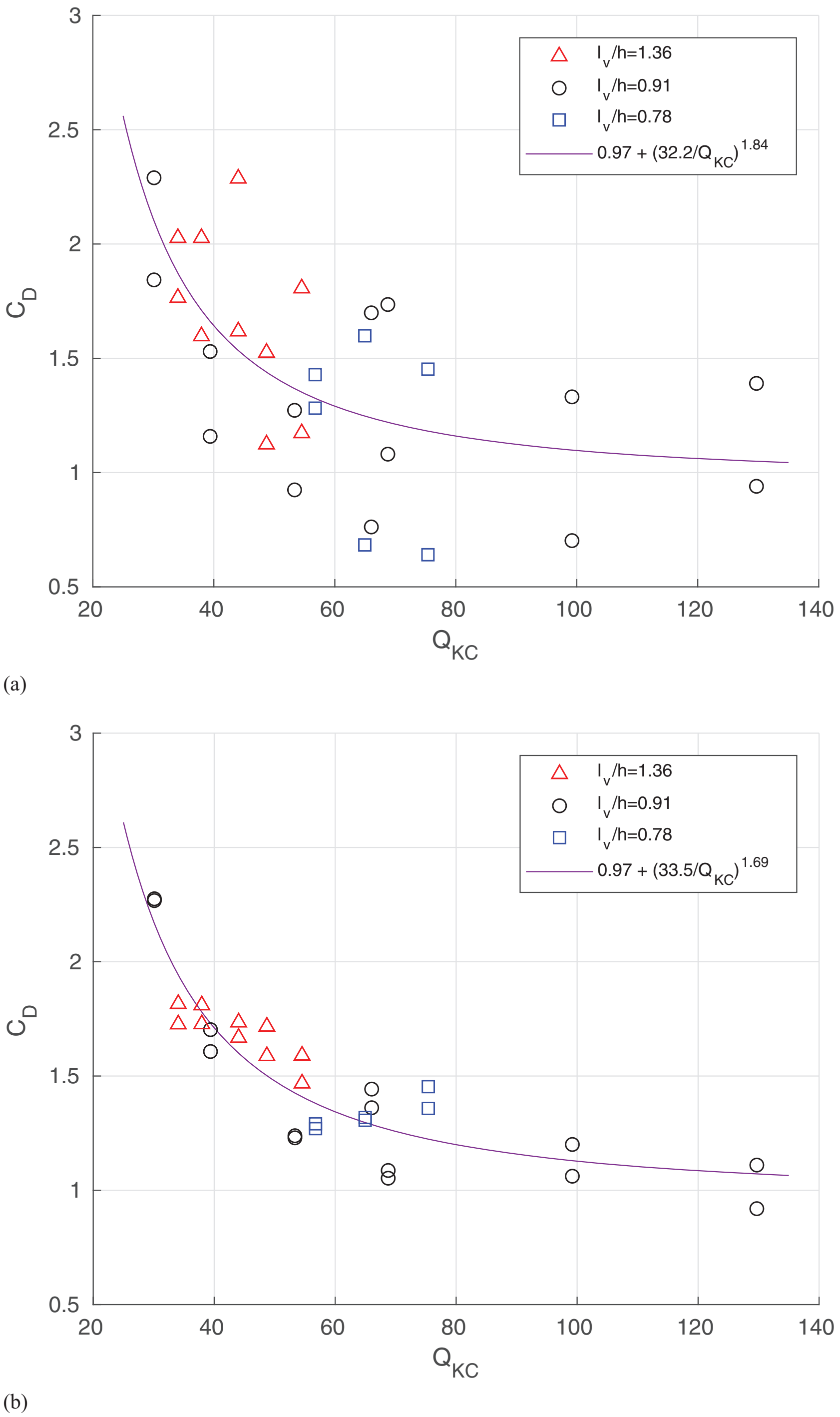

Fig. 15. Effect of modified Keulegan-Carpenter number on drag coefficient (C_D) for (a) computational wave flume; and (b) experiments. Different symbols represent different values of l_v/h.

Proteus Computational Methods and Simulation Toolkit (http://proteustoolkit.org) and is freely available. The computational wave flume reproduced the geometry and parameters of a real-world experimental wave flume. Experiments were reproduced and run for a series of scenarios with the computational wave flume. These scenarios included varying wave parameters and densities of idealized vegetative obstacles.

A full analysis of wave attenuation was performed for both the computational and experimental results, including wave-height attenuation, spectral attenuation, and wave-energy attenuation. Results from the computational wave flume were shown to adequately reproduce many experimentally observed trends. The wave-energy spectra calculated at various locations within the vegetation matched particularly well. The decay of the spectra was shown to display the same tendencies with respect to submergence ratio, relative wave height, relative depth, and stem density between the computational and experimental methods. When fit to well-known upscaling models, calculated drag coefficients, a measure of energy dissipation, produced similar curves. Analyzing such behavior is usually the only way such complex systems can be compared because pointwise values almost never match exactly between different experiments. If data sets with high-quality velocity profiles are made available, validating velocity information is an area for future work. Another potential topic of future work is to study the effects of stem–stem interaction on small-scale and bulk flow features.

Acknowledgments

Permission to publish this paper was granted by the Chief of Engineers, US Army Corps of Engineers (USACE). Funding for this work was provided by US Army Research Office Proposal 63598-MA. Work by Clint Dawson was supported by the National Science Foundation (Grant CMMI-1635115). The authors acknowledge the TACC at the University of Texas at Austin for providing high-performance computing and visualization resources that contributed to the research results reported within this paper (http://www.tacc.utexas.edu). The authors acknowledge M. E. Anderson, J. M. Smith, and the USACE Engineering Research and Development Center (ERDC) for the experimental data presented in this paper.

References

Anderson, M. E., and J. Smith. 2014. "Wave attenuation by flexible, idealized salt marsh vegetation." *Coastal Eng.* 83: 82–92. https://doi.org/10.1016/j.coastaleng.2013.10.004.

Augustin, L. N., J. L. Irish, and P. Lynett. 2009. "Laboratory and numerical studies of wave damping by emergent and near-emergent wetland vegetation." *Coastal Eng.* 56 (3): 332–340. https://doi.org/10.1016/j.coastaleng.2008.09.004.

Bradley, K., and C. Houser. 2009. "Relative velocity of seagrass blades: Implications for wave attenuation in low-energy environments." *J. Geophys. Res.: Earth Surf.* 114 (F1): F01004. https://doi.org/10.1029/2007JF000951.

Chen, H., Q. Zou, and Z. Liu. 2016a. "A coupled RANS-VOF and finite element model for wave interaction with highly flexible vegetation." *Coastal Eng. Proc.* 1 (35): 1–7. https://doi.org/10.9753/icce.v35.waves.25.

Chen, Q., and H. Zhao. 2012. "Theoretical models for wave energy dissipation caused by vegetation." *J. Eng. Mech.* 138 (2): 221–229. https://doi.org/10.1061/(ASCE)EM.1943-7889.0000318.

Chen, X., Q. Chen, J. Zhan, and D. Liu. 2016b. "Numerical simulations of wave propagation over a vegetated platform." *Coastal Eng.* 110: 64–75. https://doi.org/10.1016/j.coastaleng.2016.01.003.

Christensen, E. D. 2006. "Large eddy simulation of spilling and plunging breakers." *Coastal Eng.* 53 (5–6): 463–485. https://doi.org/10.1016/j.coastaleng.2005.11.001.

Cooper, N. J. 2005. "Wave dissipation across intertidal surfaces in the Wash Tidal Inlet, Eastern England." *J. Coastal Res.* 211: 28–40. https://doi.org/10.2112/01002.1.

Dalrymple, R., J. Kirby, and P. Hwang. 1984. "Wave diffraction due to areas of energy dissipation." *J. Waterway, Port, Coastal, Ocean Eng.* 110 (1): 67–79. https://doi.org/10.1061/(ASCE)0733-950X(1984)110:1(67).

Darby, S. 1999. "Effect of riparian vegetation on flow resistance and flood potential." *J. Hydraul. Eng.* 125 (5): 443–454. https://doi.org/10.1061/(ASCE)0733-9429(1999)125:5(443).

de Lataillade, T., A. Dimakopoulos, C. Kees, L. Johanning, D. Ingram, and T. Tezdogan. 2017. "CFD modelling coupled with floating structures and mooring dynamics for offshore renewable energy devices using the proteus simulation toolkit." In *12th European Wave and Tidal Energy Conf.* Cork, Ireland: EWTEC.

Dijkstra, J., and R. Uittenbogaard. 2010. "Modeling the interaction between flow and highly flexible aquatic vegetation." *Water Resour. Res.* 46 (12): W12547. https://doi.org/10.1029/2010WR009246.

Dimakopoulos, A. S., and A. A. Dimas. 2011. "Large-wave simulation of three-dimensional, cross-shore and oblique, spilling breaking on constant slope beach." *Coastal Eng.* 58 (8): 790–801. https://doi.org/10.1016/j.coastaleng.2011.04.002.

Dubi, A., and A. Tørum. 1996. "Wave energy dissipation in kelp vegetation." In *Proc., 25th Int. Conf. on Coastal Engineering*. Reston, VA: ASCE.

Erduran, K., and V. Kutija. 2003. "Quasi-three-dimensional numerical model for flow through flexible, rigid, submerged and non-submerged vegetation." *J. Hydroinf.* 5 (3): 189–202. https://doi.org/10.2166/hydro.2003.0015.

Fonseca, M. S., and J. A. Cahalan. 1992. "A preliminary evaluation of wave attenuation by four species of seagrass." *Estuarine Coastal Shelf Sci.* 35 (6): 565–576. https://doi.org/10.1016/S0272-7714(05)80039-3.

Gōda, Y. 2010. *Random seas and design of maritime structures.* Singapore: World Scientific. https://doi.org/10.1142/7425.

Hieu, P. D., T. Katsutoshi, and V. T. Ca. 2004. "Numerical simulation of breaking waves using a two-phase flow model." *Appl. Math. Modell.* 28 (11): 983–1005. https://doi.org/10.1016/j.apm.2004.03.003.

Hiraoka, H., and M. Ohashi. 2008. "A (k–ε) turbulence closure model for plant canopy flows." *J. Wind Eng. Ind. Aerodyn.* 96 (10–11): 2139–2149. https://doi.org/10.1016/j.jweia.2008.02.018.

Hoerner, S. 1965. *Fluid-dynamic drag: Practical information on aerodynamic drag and hydrodynamic resistance.* Wayne, PA: Hoerner Fluid Dynamics.

Ikeda, S., T. Yamada, and Y. Toda. 2001. "Numerical study on turbulent flow and honami in and above flexible plant canopy." *Int. J. Heat Fluid Flow* 22 (3): 252–258. https://doi.org/10.1016/S0142-727X(01)00087-X.

Jadhav, R. S., Q. Chen, and J. M. Smith. 2013. "Spectral distribution of wave energy dissipation by salt marsh vegetation." *Coastal Eng.* 77: 99–107. https://doi.org/10.1016/j.coastaleng.2013.02.013.

Kees, C., I. Akkerman, M. Farthing, and Y. Bazilevs. 2011. "A conservative level set method suitable for variable-order approximations and unstructured meshes." *J. Comput. Phys.* 230 (12): 4536–4558. https://doi.org/10.1016/j.jcp.2011.02.030.

Kees, C., M. Farthing, and M. Fong. 2009. *Locally conservative, stabilized finite element methods for a class of variable coefficient Navier-Stokes equations*. Technical Rep. TR-09-12. Vicksburg, MS: US Army Engineer Research and Development Center, Coastal and Hydraulics Laboratory.

Knutson, P. L., R. A. Brochu, W. N. Seelig, and M. Inskeep. 1982. "Wave damping in Spartina alterniflora marshes." *Wetlands* 2 (1): 87–104. https://doi.org/10.1007/BF03160548.

Kobayashi, N., A. Raichle, and T. Asano. 1993. "Wave attenuation by vegetation." *J. Waterway, Port, Coastal, Ocean Eng.* 119 (1): 30–48. https://doi.org/10.1061/(ASCE)0733-950X(1993)119:1(30).

Koftis, T., P. Prinos, and V. Stratigaki. 2013. "Wave damping over artificial Posidonia oceanica meadow: A large-scale experimental study." *Coastal Eng.* 73: 71–83. https://doi.org/10.1016/j.coastaleng.2012.10.007.

Krauss, K. W., T. W. Doyle, T. J. Doyle, C. M. Swarzenski, A. S. From, R. H. Day, and W. H. Conner. 2009. "Water level observations in mangrove swamps during two hurricanes in Florida." *Wetlands* 29 (1): 142–149. https://doi.org/10.1672/07-232.1.

Kubrak, E., J. Kubrak, and P. Rowiński. 2012. "Influence of a method of evaluation of the curvature of flexible vegetation elements on vertical distributions of flow velocities." *Acta Geophys.* 60 (4): 1098–1119. https://doi.org/10.2478/s11600-011-0077-2.

Kutija, V., and H. Thi Minh Hong. 1996. "A numerical model for assessing the additional resistance to flow introduced by flexible vegetation." *J. Hydraul. Res.* 34 (1): 99–114. https://doi.org/10.1080/00221689609498766.

Li, C., and J. Xie. 2011. "Numerical modeling of free surface flow over submerged and highly flexible vegetation." *Adv. Water Resour.* 34 (4): 468–477. https://doi.org/10.1016/j.advwatres.2011.01.002.

Li, C., and C. Zeng. 2009. "3D Numerical modelling of flow divisions at open channel junctions with or without vegetation." *Adv. Water Resour.* 32 (1): 49–60. https://doi.org/10.1016/j.advwatres.2008.09.005.

Lima, S. F., C. F. Neves, and N. M. L. Rosauro. 2007. "Damping of gravity waves by fields of flexible vegetation." In *Proc., Coastal Engineering 2006*, 491–503. Singapore: World Scientific.

Lowe, R. J., J. L. Falter, J. R. Koseff, S. G. Monismith, and M. J. Atkinson. 2007. "Spectral wave flow attenuation within submerged canopies:

Implications for wave energy dissipation." *J. Geophys. Res.: Oceans* 112 (C5): C05018. https://doi.org/10.1029/2006JC003605.

Luhar, M., and H. Nepf. 2016. "Wave-induced dynamics of flexible blades." *J. Fluids Struct.* 61: 20–41. https://doi.org/10.1016/j.jfluidstructs.2015.11.007.

Luhar, M., and H. M. Nepf. 2011. "Flow-induced reconfiguration of buoyant and flexible aquatic vegetation." *Limnol. Oceanogr.* 56 (6): 2003–2017. https://doi.org/10.4319/lo.2011.56.6.2003.

Manca, E., I. Cáceres, J. Alsina, V. Stratigaki, I. Townend, and C. Amos. 2012. "Wave energy and wave-induced flow reduction by full-scale model Posidonia oceanica seagrass." *Cont. Shelf Res.* 50–51: 100–116. https://doi.org/10.1016/j.csr.2012.10.008.

Mattis, S. A. 2013. "Mathematical modeling of flow through vegetated regions." Ph.D. thesis, Univ. of Texas at Austin. http://hdl.handle.net/2152/21165.

Mattis, S., C. Dawson, C. Kees, and M. Farthing. 2012. "Numerical modeling of drag for flow through vegetated domains and porous structures." *Adv. Water Resour.* 39: 44–59. https://doi.org/10.1016/j.advwatres.2012.01.002.

Mattis, S. A., C. N. Dawson, C. E. Kees, and M. W. Farthing. 2015. "An immersed structure approach for fluid-vegetation interaction." *Adv. Water Resour.* 80: 1–16. https://doi.org/10.1016/j.advwatres.2015.02.014.

Maza, M., J. L. Lara, and I. J. Losada. 2013. "A coupled model of submerged vegetation under oscillatory flow using Navier–Stokes equations." *Coastal Eng.* 80: 16–34. https://doi.org/10.1016/j.coastaleng.2013.04.009.

Mei, C. C., I.-C. Chan, P. L.-F. Liu, Z. Huang, and W. Zhang. 2011. "Long waves through emergent coastal vegetation." *J. Fluid Mech.* 687: 461–491. https://doi.org/10.1017/jfm.2011.373.

Mendez, F. J., and I. J. Losada. 2004. "An empirical model to estimate the propagation of random breaking and nonbreaking waves over vegetation fields." *Coastal Eng.* 51 (2): 103–118. https://doi.org/10.1016/j.coastaleng.2003.11.003.

Meneveau, C., and T. Lund. 1997. "The dynamic Smagorinsky model and scale-dependent coefficients in the viscous range of turbulence." *Phys. Fluids* 9 (12): 3932–3934. https://doi.org/10.1063/1.869493.

Möller, I., and T. Spencer. 2002. "Wave dissipation over macro-tidal saltmarshes: Effects of marsh edge typology and vegetation change." *J. Coastal Res.* 36: 506–521. https://doi.org/10.2112/1551-5036-36.sp1.506.

Peskin, C. 2002. "The immersed boundary method." *Acta Numer.* 11 (1): 479–517.

Quartel, S., A. Kroon, P. Augustinus, P. Van Santen, and N. Tri. 2007. "Wave attenuation in coastal mangroves in the Red River Delta, Vietnam." *J. Asian Earth Sci.* 29 (4): 576–584. https://doi.org/10.1016/j.jseaes.2006.05.008.

Sánchez-González, J. F., V. Sánchez-Rojas, and C. D. Memos. 2011. "Wave attenuation due to Posidonia oceanica meadows." *J. Hydraul. Res.* 49 (4): 503–514. https://doi.org/10.1080/00221686.2011.552464.

Saowapon, C., and N. Kouwen. 1989. "Physically based model for determining flow resistance and velocity profiles in vegetated channels." *Symposium on Manning's Equation*, edited by B. C. Yen, 559–568. Charlottesville, Virginia: Univ. of Virginia.

Smith, J. M., R. E. Jensen, A. B. Kennedy, J. C. Dietrich, and J. J. Westerink. 2011. "Waves in wetlands: Hurricane Gustav." *Coastal Eng. Proc.* 1 (32): 1–12. https://doi.org/10.9753/icce.v32.waves.29.

Stratigaki, V., E. Manca, P. Prinos, I. J. Losada, J. L. Lara, M. Sclavo, C. L. Amos, I. Cáceres, and A. Sánchez-Arcilla. 2011. "Large-scale experiments on wave propagation over Posidonia oceanica." *J. Hydraul. Res.* 49 (Supp1): 31–43. https://doi.org/10.1080/00221686.2011.583388.

Tahvildari, N. 2017. "Numerical modeling of the interactions between nonlinear waves and arbitrarily flexible vegetation." *Coastal Eng. Proc.* 1 (35): 1–11. https://doi.org/10.9753/icce.v35.waves.32.

Timoshenko, S. 1956. *Strength of materials: Advanced theory and problems.* New York: D. Van Nostrand Company.

Velasco, D., A. Bateman, and V. Medina. 2008. "A new integrated, hydromechanical model applied to flexible vegetation in riverbeds." *J. Hydraul. Res.* 46 (5): 579–597. https://doi.org/10.3826/jhr.2008.2986.

Voke, P. 1996. "Subgrid-scale modelling at low mesh Reynolds number." *Theor. Comput. Fluid Dyn.* 8 (2): 131–143. https://doi.org/10.1007/BF00312367.

Wayne, C. 1976. "The effects of sea and marsh grass on wave energy." *Coastal Res. Notes* 4 (7): 6–8.

Wu, W., et al. 2011. *Investigation of surge and wave reduction by vegetation*. Phase I Rep. for SERRI Project No. 80037, 315. University, MS: National Center for Computational Hydroscience and Engineering, Univ. of Mississippi.

Zeller, R. B., J. S. Weitzman, M. E. Abbett, F. J. Zarama, O. B. Fringer, and J. R. Koseff. 2014. "Improved parameterization of seagrass blade dynamics and wave attenuation based on numerical and laboratory experiments." *Limnol. Oceanogr.* 59 (1): 251–266. https://doi.org/10.4319/lo.2014.59.1.0251.

Zhu, L., and Q. Chen. 2015. "Numerical modeling of surface waves over submerged flexible vegetation" *J. Eng. Mech.* 141 (8): A4015001. https://doi.org/10.1061/(ASCE)EM.1943-7889.0000913.

Zhu, L., and Q. Chen. 2017. "Attenuation of nonlinear waves by rigid vegetation: Comparison of different wave theories." *J. Waterway, Port, Coastal, Ocean Eng.* 143 (5): 04017029. https://doi.org/10.1061/(ASCE)WW.1943-5460.0000415.